Accepted Manuscript

Micromachined nanocrystalline graphite membranes for gas separation

S.J. Fishlock, S.H. Pu, G. Bhattacharya, Yisong Han, J. McLaughlin, J.W. McBride, H.M.H. Chong, S.J. O'Shea

Please cite this article as: S.J. Fishlock, S.H. Pu, G. Bhattacharya, Y. Han, J. McLaughlin, J.W. McBride, H.M.H. Chong, S.J. O'Shea, Micromachined nanocrystalline graphite membranes for gas separation, *Carbon* (2018), doi: 10.1016/j.carbon.2018.05.071.

Micromachined nanocrystalline graphite membranes for gas separation

S.J. Fishlock[1-5*], S.H. Pu[1,3,4], G. Bhattacharya[5,6], Yisong Han[5], J. McLaughlin[5], J.W. McBride[1,3], H.M.H. Chong[4] and S.J. O' Shea[2].

[1]Mechatronics Research Group, Faculty of Engineering and the Environment, University of Southampton, Southampton SO17 1BJ, UK

[2] A*STAR, Institute of Materials Research and Engineering (IMRE) 2 Fusionopolis Way, Innovis, Singapore, 138634

[3]University of Southampton Malaysia Campus, Iskandar Puteri, 79200, Johor, Malaysia

[4]Sustainable Electronic Technologies Research Group, School of Electronics and Computer Science, University of Southampton, Southampton SO17 1BJ, UK

[5]Nanotechnology Integrated Bio-Engineering Centre, University of Ulster, Shore Road, BT37 0QB Newtownabbey, United Kingdom

[6]Department of Physics, School of Natural Sciences, Shiv Nadar University, Gautam Buddha Nagar 201314, Uttar Pradesh, India.

*Corresponding author. Tel +442890368433. E-mail s.fishlock@ulster.ac.uk

Micromachined nanocrystalline graphite membranes for gas separation

S.J. Fishlock[1-5*], S.H. Pu[1,3,4], G. Bhattacharya[5,6], Yisong Han[5], J. McLaughlin[5], J.W. McBride[1,3], H.M.H. Chong[4] and S.J. O'Shea[2].

[1]Mechatronics Research Group, Faculty of Engineering and the Environment, University of Southampton, Southampton SO17 1BJ, UK

[2] A*STAR, Institute of Materials Research and Engineering (IMRE) 2 Fusionopolis Way, Innovis, Singapore, 138634
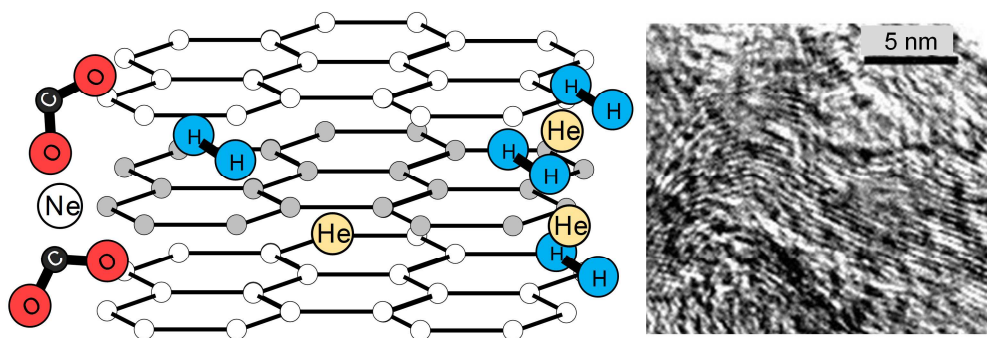
[3]University of Southampton Malaysia Campus, Iskandar Puteri, 79200, Johor, Malaysia

[4]Sustainable Electronic Technologies Research Group, School of Electronics and Computer Science, University of Southampton, Southampton SO17 1BJ, UK

[5]Nanotechnology Integrated Bio-Engineering Centre, University of Ulster, Shore Road, BT37 0QB Newtownabbey, United Kingdom

[6]Department of Physics, School of Natural Sciences, Shiv Nadar University, Gautam Buddha Nagar 201314, Uttar Pradesh, India.

Abstract

Carbon nanoporous membranes show promising performance for the passive separation and sieving of different gases, for example for helium and hydrogen separation. In this paper, nanocrystalline graphite (or nanographite) has been evaluated as a membrane material for molecular sieving of helium and hydrogen from larger gas constituents. Nanographite of 350 nm thickness was prepared using plasma-enhanced chemical vapour deposition onto fused silica substrates, from which membranes were microfabricated using deep wet etching. Permeability of hydrogen and helium were 1.79×10^{-16} and 1.40×10^{-16} $mol \cdot m \cdot m^{-2} \cdot s^{-1} \cdot Pa^{-1}$ at 150 °C respectively, and measured separation was 48 for He/Ne, >135 for H_2/CO_2 and >1000 for H_2/O_2. The gas separation properties of the nanographite membranes were tested in the temperature range of 25 to 150 °C, and the permeation measurements show nanographite to be highly selective of helium and hydrogen over all larger gas molecules, including neon.

*Corresponding author. Tel +442890368433. E-mail s.fishlock@ulster.ac.uk (Sam Fishlock)

1. **Introduction**

Nanoporous membranes are attractive candidates for use as molecular sieves for the separation of helium and hydrogen from the larger constituents of natural gas [1,2]. Helium is an irreplaceable natural resource which is widely used in many industrial and scientific applications such as cryogenics and CMOS fabrication [1]. Helium is commonly extracted from fields of natural gas using cryogenic processing, whereby the mixture of gases is separated cryogenically [3]. This highly energy intensive process is often not financially viable and in many cases the helium is permanently lost to atmosphere [4], and as a result, less energy-intensive methods of helium extraction are sought, and molecular sieving using membranes is considered a promising method of production. Similarly, hydrogen is an important fuel and is also generally obtained from, for example, natural gas and bioethanol, which leaves hydrogen in a mixture of undesired products such as CO_2, CH_4 and CO which need to be further separated [5,6].

Several theoretical studies have shown the promise of 2D materials such as graphene [7], graphdiyne [8], carbon nitride [9] and silicene [10] to be used as molecular sieves for helium and hydrogen separation. These simulations show that the intrinsic pores in 2D materials caused by vacancies such as Stone-Wales defects and pores could enable membranes with very high flux of helium or hydrogen, combined with high separation from all other gases [7]. However, the prospect of fabricating robust, temperature resistant, large-area 2D films, with the presence of solely specific and 'tailored' defects (as opposed to non-specific defects and pores) remains somewhat distant. For example, studies of the gas transport through stacked graphene sheets have shown that tears and unintended defects greatly reduce the sieving properties of membranes [11].

As a result of the potential challenges facing the upscaling of 'pure' 2D thin films, related porous materials such as thin graphite oxide or graphene oxide [12,13] are considered to be promising molecular sieve materials, as this has more scalable and reproducible production, and is more viable to be used in large-scale applications. However the behaviour of graphene oxide molecular sieves currently show a small window of operation regarding temperature; with the separation factor of hydrogen and carbon dioxide ($\alpha^{H_2}/_{CO_2}$) for 1.8 nm thick membranes, falling from ~ 2090 at 20 °C to ~ 22 at 100 °C [13]. A similar result was observed in graphene oxide membranes by Chi *et al.* with $\alpha^{H_2}/_{CO_2}$ falling from 240 at room

temperature to 47 at 120 °C [14]. As a result, a wider range of carbon materials are sought as molecular sieves due to their high flux and temperature resistance [2]. Recent studies on carbon materials have included pressed graphite [5] turbostratic and amorphous carbon [15], graphite foils [16], carbon nanomembranes derived from terphenylthiol [17] and polymer-derived carbons [18].

Furthermore, micromachined and miniaturised membranes for hydrogen separation are of specific interest in the use of micro-generators based on hydrogen production in micro-reactors [19–21]. In such systems, hydrogen is produced from steam reforming of methane [20] or catalytic reaction from methanol [21]. This chip-scaled power enables a high-density and high efficiency power source, which is required in certain aerospace [19] and consumer electronics [21] applications. High purification and separation of hydrogen from larger gas constituents are required to help bring such micro-reactor generators to wider use. Currently, such micro-reactors have typically relied on hydrogen separation using palladium membranes [19–21] which are highly expensive, and suffer excessive sensitivity to surface contamination [2].

In this study, we explore the use of thin-film nanocrystalline graphite (referred to as NCG, nanographene or nanographite) micro-scaled membranes, as a candidate material for helium and hydrogen separation. Nanographite has crystallite sizes of roughly ~ 2 to 50 nm [22–24]. One advantage of nanographite is that it may be deposited onto large-area substrates using plasma-enhanced chemical vapour deposition (PECVD) without any metal catalyst; this enables fabrication and characterisation of freestanding membranes using MEMS-type technology such as lithographic patterning and etching. Here, we demonstrate a method to fabricate freestanding thin-film membranes using deep HF etching which may be used for batch production of micro-scaled membranes. We present the gas permeation and separation behaviour of nanographite membranes in the temperature range of 25 to 150 °C, and demonstrate this to be a promising membrane material with high sieving behaviour, inexpensive, large area synthesis and preparation, and potential for micro-scaled applications.

2. **Experimental**

2.1 Deposition of nanographite

3

Nanographite was deposited onto a 4-inch fused silica wafer (University Wafers, USA), using a commercial PECVD tool (Oxford Instruments Nanofab1000 Agile), with a methane precursor and hydrogen diluent at a temperature of 750 °C. The further deposition conditions, and detailed mechanical characterisation have been described in previous work by our group [24–26].

2.2 Material characterisation

Raman spectroscopy (Renishaw inVia) was used to characterise the structural properties of the nanographite film, using a 532 nm wavelength excitation laser and 50 × magnification. Scanning electron microscopy (JEOL JSM 6700F, 5.0 kV accelerating voltage) was used to view the morphology of the film on the as-deposited fused silica substrate. Grazing angle X-ray diffraction was performed (Bruker D8) using a CuK_α source with wavelength of 0.154 nm. TEM samples were prepared using mechanical exfoliation into ethanol, sonicated for 10 minutes and micropipetted onto copper-supported holey carbon grids (Agar Scientific Holey carbon film on 300 mesh cu). HRTEM (JEOL JEM-2100F) was used for imaging at 200 keV excitation.

2.3 Microfabrication of membranes

To fabricate a membrane, nanographite was deposited to a thickness of 350 nm onto one side of a double-polished 4-inch fused silica wafer. The nanographite was annealed at a temperature of 1000 °C for one minute under N_2 flow, after vacuum evacuation, using a rapid thermal annealer (Jipelec JetFirst 150) to reduce the compressive stress of the film. Without the annealing step, a high level of buckling and breakage was observed. A chrome/gold (10/300 nm thickness) mask was patterned on the wafer back side using thermal evaporation (Fig. 1 (A)), over which a 7 µm layer of AZ4330 resist was spun, and patterned with a circular window of 25 µm diameter, Fig. 1 (B). The wafer was then post-baked for 20 minutes at 120 °C in an oven. This post-bake was used to make the resist layer more hydrophobic [27] and thus reduce pinhole damage to the gold mask from the later deep hydrofluoric acid (HF) etch. The chrome/gold mask was etched using Aldrich gold etchant and Microchrome Technology, CEP-200 chrome etchant respectively.

4

The wafer was then diced and the front side of each membrane chip was protected from the HF by adhering the surface to a silicon wafer using melted wax, heated at 50 °C and then left to cool at room temperature. 49 % HF acid was used to isotropically etch the fused silica through to the nanographite, thus releasing the membrane, Fig. 1 (C). The etching process typically took around 12 to 16 hours. After etching, the wax was melted and the chip thoroughly cleaned in, successively, acetone, deionised water and isopropyl alcohol, Fig. 1 (D). A microscope image of a released membrane is shown in Fig. 2. The membrane is slightly buckled due to some remaining compressive stress, but remained fairly robust. This fabrication process gave reproducible results, with around 75 % of 100 – 1000 µm diameter membranes successfully released.
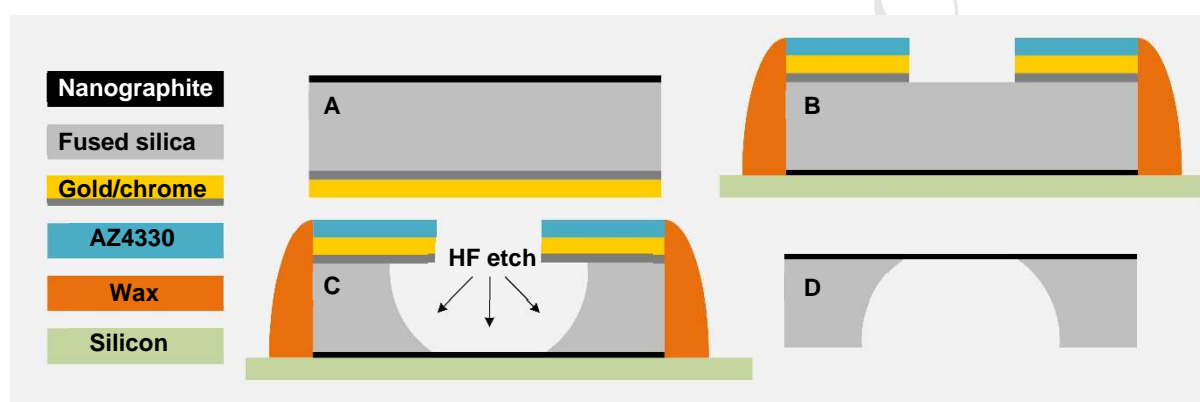

Fig. 1. Schematic fabrication process of nanographite membranes on fused silica substrates. (A) Deposition of nanographite using PECVD and Cr/Au using thermal evaporation. (B) Photolithography using AZ4330 resist followed by Au and Cr etching, front protection using wax and a silicon carrier. (C) Deep HF etching. (D) Wax melting and solvent cleaning.
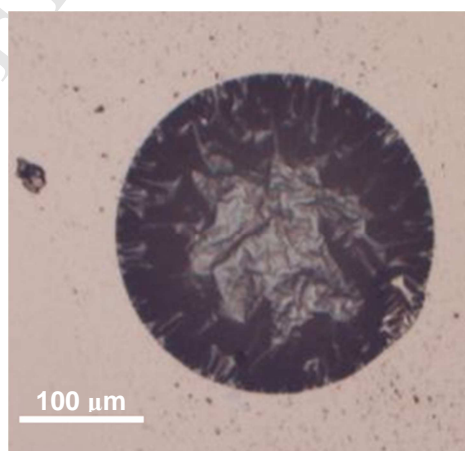

Fig. 2. Microscope image of a released nanographite membrane taken from the top side. The membrane shows slight crumpling due to some compressive stress.

2.4   Mass spectrometry system for permeance measurement

The flux of gases through the membrane was calculated by measuring the downstream pressure of gas using a residual gas analyser (RGA, SRS RGA 300) type quadrupole mass spectrometer in an ultra-high vacuum (UHV) chamber. Fig. 3 shows a schematic of the system, and is similar to permeation testing rigs used in other reports [28,29].
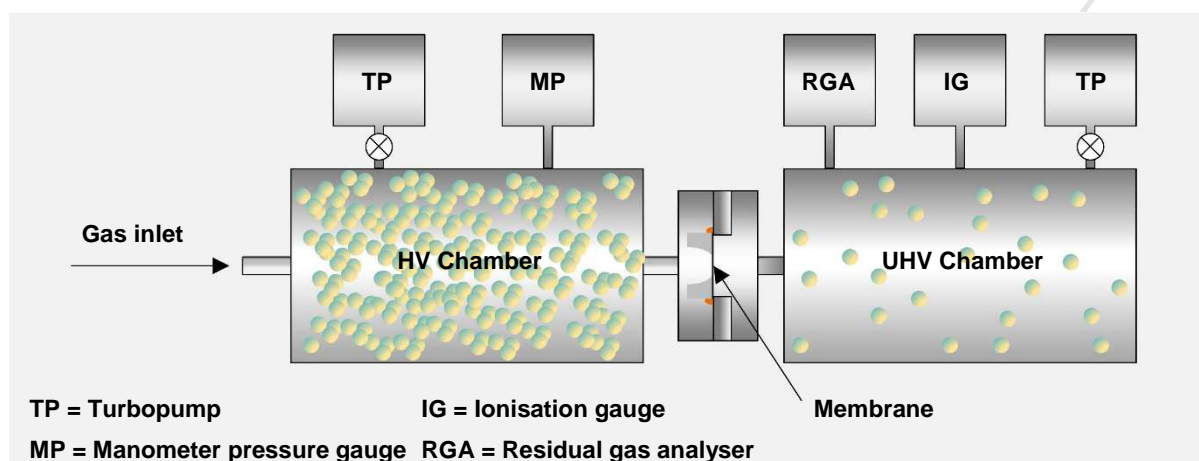

Fig. 3. Schematic of UHV rig used to measure the permeance of nanographite membranes.

The rig comprises two chambers, separated by the membrane. The larger chamber (6.74 L volume) is at ultrahigh vacuum (UHV) in which sensitive gas partial pressure measurements are made using the RGA, and a smaller chamber evacuated to high vacuum (HV), which during testing is filled with the analyte gas to a pressure up to 80 Torr. The membrane was sealed over a 1/4'' stainless steel Swagelok gasket using a UHV-rated 2-part adhesive (Allectra 330s-GLUE1-M3). The gasket was then adhered using the same adhesive over the orifice connecting the two chambers. The UHV chamber was evacuated using a Varian V-551 turbomolecular pump rated to 550 L s^{-1}. The system was thoroughly baked overnight using external heater tapes at 150 °C to remove water vapour and other contaminants from the system walls. After baking, a UHV base pressure of around 1×10^{-10} Torr was achieved. The two chambers are separated by the membrane, and gas flows through due to the concentration gradient. To measure the flux through the membrane, the UHV chamber was shut off from the evacuating turbopump and the pressure rise of the analyte gas was measured until the overall pressure in the UHV chamber reached around 1×10^{-5} Torr. During measurement, only the pressure of the analyte gas was measured, as the RGA enables measurement of the ion current at a specified atomic mass, whilst ignoring the pressure of

other background gases. The RGA was calibrated against a total-pressure ionisation gauge [30].

To test the leak-tightness of the membrane holder, a blank (plain fused silica chip) was adhered over a gasket, and helium was flowed to a pressure of 80 Torr to the HV side of the setup and the pressure observed using the RGA. No pressure rise of helium was observed, showing that during testing all flowing gas should be through the membrane itself. To measure the flux of gases through the membrane at elevated temperature, the membrane holder and adjacent components were wrapped in heating tape and aluminium foil, to help maintain homogenous heating throughout. A thermocouple was taped to the outer face of the membrane holder using conductive carbon tape and the sample was heated and maintained at temperature for one hour prior to permeation measurement. The measurement of helium, hydrogen, neon, oxygen and carbon dioxide was performed through a nanographite membrane at temperatures from room temperature (25 °C) to 150 °C.

2.5   Gas flux measurement

The membrane leak rate Q_m (Pa $\cdot$ m^3 $\cdot$ s^{-1}) can be calculated by measuring the change in partial pressure of the analyte gas with time, as described in Equation 1 [31]:

$$Q_m = \left[\left(\Delta P_{avg} / \Delta t \right) - \left(\Delta P_0 / \Delta t \right) \right] \cdot v \tag{1}$$

where ΔP_{avg} is the measured change in pressure over a time period Δt, ΔP_0 is the measured change in background pressure arising from gases emanating from the vacuum chamber internal surfaces and v is the measured volume of the chamber. This pressure rise occurs in the UHV system, when the turbopump valve has been closed, to allow the analyte gas pressure to build up. ΔP_0 was measured from the background signal, by measuring the pressure rise when there was no analyte gas present in the HV chamber. ΔP_0 was negligible in the case of helium, since there is no ambient helium present in the UHV chamber, however ΔP_0 was non-negligible in the case of hydrogen, since some hydrogen diffuses from the inner steel walls of the UHV chamber, particularly from the grain boundaries [32]. From the leak rate, the molar flux, J, (mol m^{-2}s^{-1}) may be calculated by [31]:

$$J = Q_m / RTa \tag{2}$$

where a is the geometric surface area of the membrane, R is the molar gas constant and T is the absolute temperature. The permeance, B, (mol $\cdot$ m^{-2} $\cdot$ s^{-1} $\cdot$ Pa^{-1}) is defined as [33]:

$$B = J / P_{hv} \tag{3}$$

where P_{hv} is the upstream pressure of the gas, in the HV chamber. The coefficient of permeability C (mol $\cdot$ m $\cdot$m^{-2} $\cdot$ s^{-1} $\cdot$ Pa^{-1}) is a measure of the thickness-normalised permeance of a membrane material [34] and is calculated as:

$$C = B \cdot x \tag{4}$$

where x is the membrane thickness. The selectivity α of two gases is calculated as the ratio of the permeance of both gases, flowing under the same conditions:

$$\alpha = \frac{B_1}{B_2} \tag{5}$$

3   Results and discussion

3.1 Material characterisation

Nanocrystalline graphite comprises nano-scaled crystallites of sp^2 bonded carbon [35,36]. A Raman spectrum obtained from a nanographite thin film is shown in Fig. 4, with the main peaks highlighted. The characteristic D peak (A$_{1g}$ breathing mode 1350 cm^{-1}) arises from defects such as grain boundaries and dislocations in the graphitic structure, and is characteristic of defected graphene or graphite [37] and the G peak (E$_{2g}$ mode 1594 cm^{-1}) is the so-called 'graphite mode' and originates from the radial breathing mode of sp^2 carbon [37]. The 2D peak (second order of the D peak of 2690 cm^{-1}) is an overtone of the D peak [38]. The D+G peak (2934 cm^{-1}) is defect related [39]. To calculate I_D/I_G we fit Lorentzian peaks (Origin Pro 9.3) to the D and G peaks, with a Fano peak for the slight shoulder of D' (1620 cm^{-1})   [24,39] and I_D/I_G equals ~1.79 which is characteristic of a nanocrystalline graphite [37]. An SEM image of nanographite is included in Fig. 5, which shows the granular structure of nanographite.
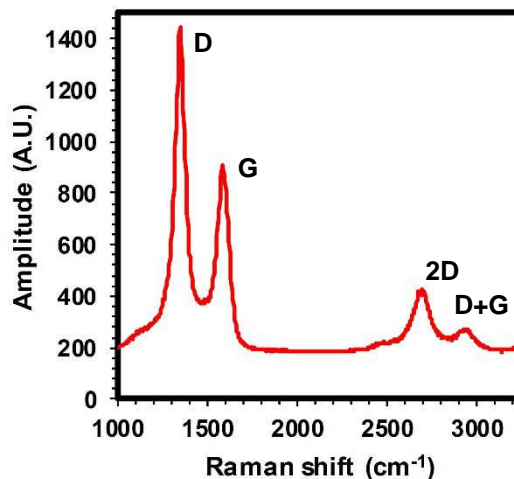
Fig. 4. Raman spectrum of 350 nm thick nanographite sample, on a fused silica substrate with the main peaks denoted.
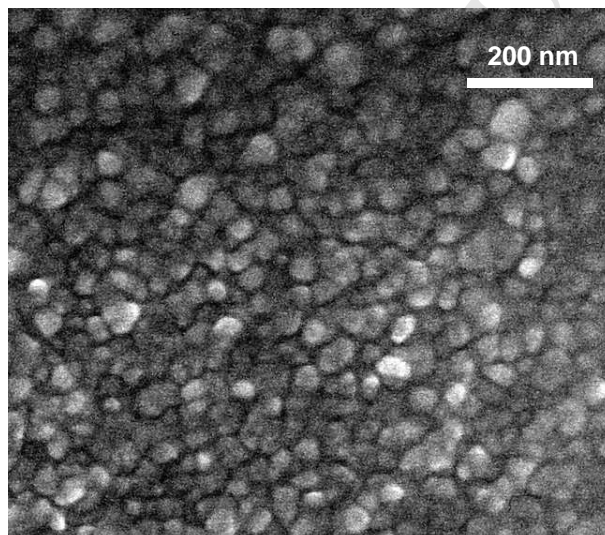

Fig. 5. SEM image of nanographite morphology on fused silica substrate.

X-ray diffraction (XRD) was carried out to confirm the presence of graphitic phases. The XRD pattern of nanocrystalline graphite deposited on fused silica substrate is shown in Fig. 6. The plot mainly consists of two broad peaks centered at $2\theta \sim 21.8^{\circ}$ and $2\theta \sim 43.7^{\circ}$. The first peak can be attributed to the fused silica substrate, as observed previously [40]. In order to confirm that the peak arises because of the substrate, a similar grazing angle XRD was also carried out on the pristine substrate, shown in Fig. 6, and a similar peak is obtained. The second XRD peak around $2\theta \sim 43.7^{\circ}$ can be assigned to the graphite (100) crystal plane [40]

9

with some inherent strain. In order to calculate the hexagonal spacing we used Bragg's equation [41]:

$$2d \sin \theta = n\lambda \qquad (6)$$

where θ is half of the diffraction angle, n equals 1 and λ is the wavelength of X-rays (0.154 nm). The hexagonal spacing (d_{100}) is calculated as ~0.21 nm which corresponds closely to similar studies on nanographite [42]. Because of the lack of long range crystallinity of the nanographite, a very high fullwidth at half maximum (FWHM) (~0.05 radian) is obtained. The crystallite size was further calculated using the Scherrer equation [43]:

$$D = \frac{k\lambda}{\beta \cos \theta} \qquad (7)$$

where D is the average crystalline size, k is a constant (k=0.89), λ is the wavelength of X-rays (0.154 nm), β is the FWHM of the diffraction peak and θ is half of the diffraction angle. The average crystalline size is calculated, and the value of D is found to be ~ 3.0 nm, which is similar to the crystallite size measured by Hargreaves *et al.* [42] who measured a mean graphene domain size of ~ 1 to 3 nm, with some larger crystallites.

Fig. 6. X-ray diffraction patterns of the nanographite sample on fused silica substrate, and the bare silica substrate.

TEM analysis is shown in Fig. 7 (A-D), of an exfoliated flake suspended on a holey carbon grid. From the bright-field TEM images shown in Fig. 7(A-B), we observe that nanographite is comprised of planar sheets, randomly oriented. Fig. 7(C) is a HRTEM image, and here we observe nano-sized graphitic crystallite regions with no long-range order. The nano-scaled

10

crystallites are of random orientation and range from a few to ~ 20 graphitic layers, which appears broadly consistent with the crystallite size obtained from XRD (~ 3 nm). The interlayer spacing d_{002} was measured using selected-area electron diffraction (SAED), Fig. 7 (D), and shows interlayer graphite spacing of 0.34 nm, similar to previous measurements of between 0.34 and 0.345 nm [42,44] for nanographite. We were not able to calculate a value of (d_{002}) from XRD as this was largely masked by the substrate. The hexagonal spacing (d_{100}) was measured from SAED as 0.21 nm, in close agreement with the XRD value.
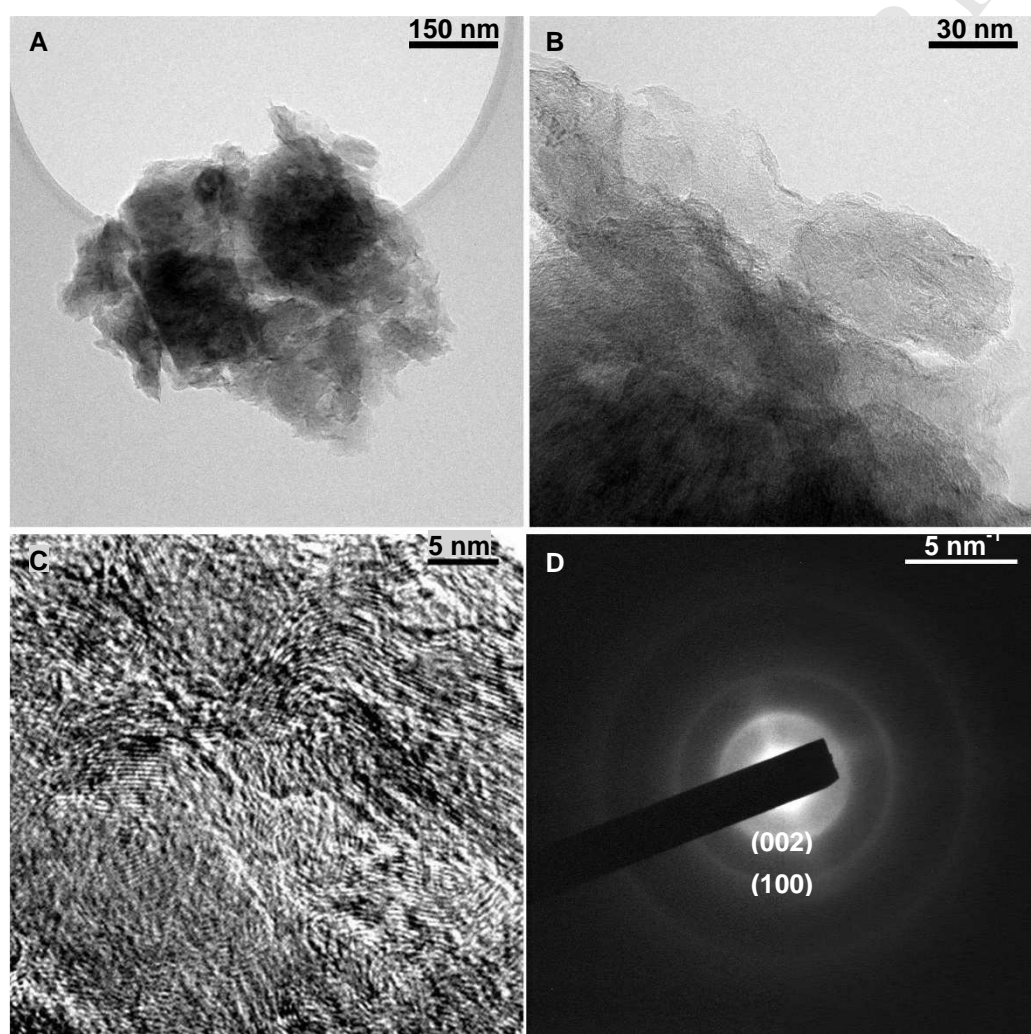

Fig. 7. (A-B) Bright field TEM images of nanographite sample suspended on a holey carbon grid (C) HRTEM images of a nanographite sample (D) Selected-area electron diffraction pattern, taken from the suspended region of the sample, shows hexagonal spacing (d_{100}) of 0.21 nm and interlayer spacing (d_{002}) of 0.34 nm.

11

The graphitic structure acts as a molecular sieve, as the interlayer spacing may be small enough to allow flow of the smallest gases (helium, hydrogen and neon, summarised in Table 1), but acts as a far greater barrier to larger gases such as CO_2 and O_2 [45–47]. The diffusion of hydrogen in between graphite sheets has previously been simulated [48]. Nanographite also includes some amorphous bonding, but previous measurements have shown that amorphous carbon does not have very high gas separation properties [15], with $\alpha^{H_2}/_{CO_2}$ measured at ~2.8 between the temperature range 25 to 250 °C and sieving is expected to be dominated by the interlayer graphitic spacing. Previously the interlayer permeation of hydrogen through pressed graphite membranes was shown to have a significant effect on overall flow, in which the permeation parallel to the grains was a factor of around 25 higher than that perpendicular to the grains [5] . Shen *et al.* [47] showed that the 0.35 nm spacing between graphene oxide sheets provided transport channels with high separation properties. However, for graphene-oxide, the selectivity may also apparently be altered through different preparation techniques, Li *et al.* [13] observed gas selectivity through a different mechanism of gas flow through pores and defects at the grain boundaries with no major increase in flow observed with increased interlayer spacing.

3.2   Separation performance

Initially, the single-gas permeance of helium, hydrogen and neon was measured through a nanographite membrane over the temperature range 25 to 150 °C, with permeance values shown in Fig. 8 (A). Note the much lower value of permeance for neon, as detailed in the inset of Fig. 8(A). For each gas, the permeance increases exponentially with temperature. Fig. 8 (B) is an Arrhenius plot showing the permeance against the inverse of temperature, which can be used to calculate activation energy which is shown in Table 1.
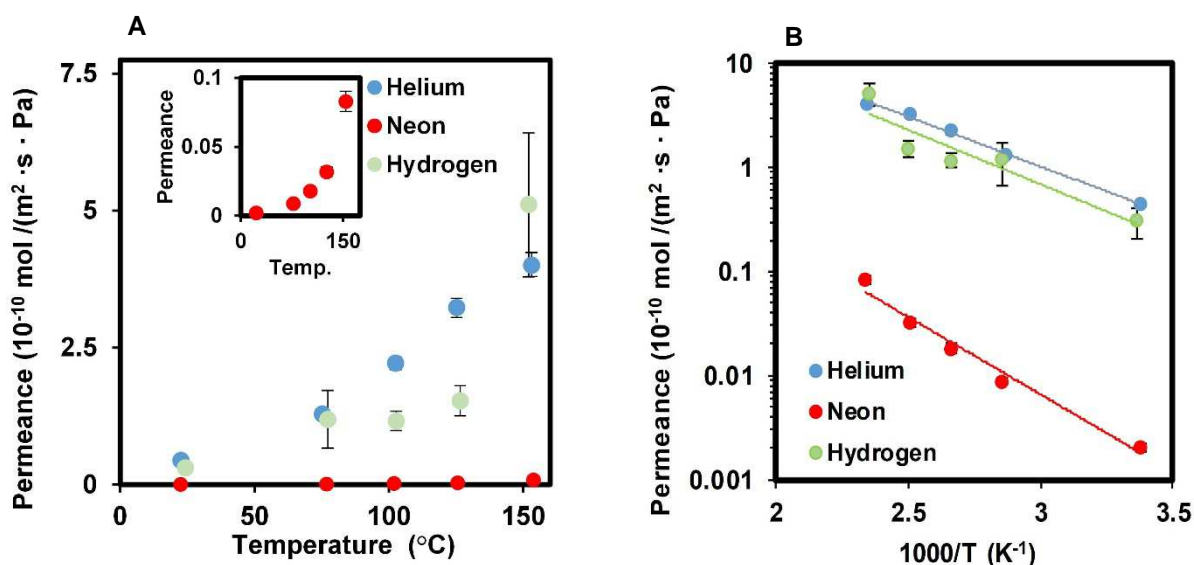
Fig. 8. (A) Measurement of the permeance of helium, hydrogen and neon through a 350 nm thick nanographite membrane across the temperature range of 25 to 150 °C. Inset shows values of neon permeance in detail, as the permeance is much lower than of the other gases. (B) Arrhenius plot of the same data enables calculation of the activation energy of each gas.

Gas	Activation energy (kJ/Mol)	Molecular diameter (nm)
Helium	18.31	0.260 [49]
Hydrogen	20.03	0.289[49]
Neon	28.50	0.275[50]
Carbon Dioxide	-	0.339 [49]
Oxygen	-	0.346 [51]

Table 1. The calculated values of activation energy, and values of molecular diameter for five measured gases.

The temperature dependent selectivity plot of α^{He}_{Ne}, and $\alpha^{H_2}_{Ne}$ is shown in Fig. 9. At room temperature α^{He}_{Ne} and $\alpha^{H_2}_{Ne}$ are 212 and 146, respectively. There is a clear decrease in the selectivity as the temperature increases; with $\alpha^{He}_{Ne} = 48$ and $\alpha^{H_2}_{Ne} = 62$ at 150 °C. The reason for this behaviour is simply that neon has a higher activation energy than helium or hydrogen, and thus its permeance increases relatively more at higher temperatures.

13

To test the permeance of larger gases, the permeance of carbon dioxide and oxygen were measured through a nanographite membrane. However, the permeation of both gases through the nanographite membrane was below the limit of detection of the mass spectrometry system. Low amounts of both gases were detected from the background of the UHV system (for example CO_2 is known to diffuse from the inner steel walls [32]). However, the amount diffusing through the membrane did not raise the measured value of either of these gases. As a result, no absolute values of gas permeation and separation were obtained, but a lower limit for separation factors of greater than ~135 and ~1000, respectively, can be ascertained for hydrogen over both CO_2 and O_2, as any higher values would have been easily measured above the background. This appears to indicate that there is a cut-off of permeance between hydrogen (0.289 nm) and CO_2 (0.339 nm) as the permeance greatly differs between these two gases. This may suggest that the flow of gases through nanographite is predominantly interlayer rather than through inter-grain defects since the drop-off in permeance appears to lie close to the interlayer spacing size (0.34 nm).
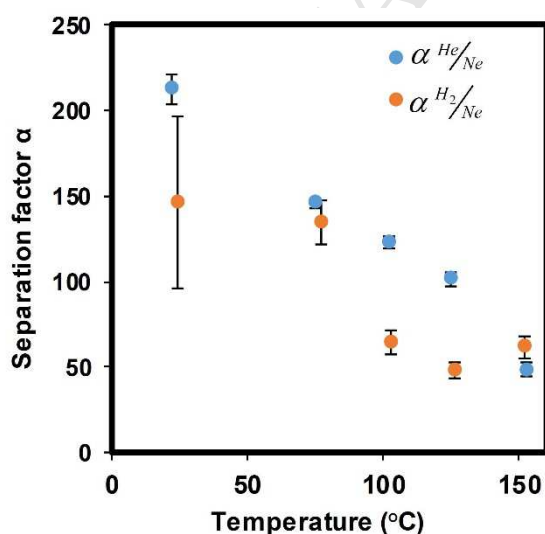
Fig. 9. Calculated values of separation factors $\alpha^{He}/_{Ne}$ and $\alpha^{H_2}/_{Ne}$ over the temperature range of 25 to 150 °C.

3.3   Discussion of separation behaviour

In inorganic membranes, the transport tends to be dominated by the following mechanisms: Knudsen diffusion, surface diffusion, or sized-based molecular sieving (also termed gas translation diffusion) [45,52–54]. In relatively large pores, the transport is dominated by the mean-free-path of the molecule, which is known as Knudsen diffusion [52]. However, in the present membranes, the ratio of permeance for both $\alpha^{He}/_{Ne}$ and $\alpha^{H_2}/_{Ne}$ is far higher than that

14

predicted by Knudsen diffusion, which may be calculated from the molecular mass M of either constituent, for example ($\alpha_{Knudsen}\ ^{He}\!/\!_{Ne} = \sqrt{M_{Neon} / M_{Helium}} = 2.2$). For smaller pores, the flow may be dominated by surface diffusion [45] where molecules adsorb on to the pore walls, before hopping to the next available site [50]. As temperature increases, the adsorption decreases and thus the permeance from surface diffusion flow will also decrease [55], which is not observed in any significant way in our data.

Hence, for the nanographite membrane, the flow is probably dominated by molecular sieving (gas translation diffusion) for the smallest pores as has been previously noted in various carbon-based membranes [45,53]. In gas translational diffusion, there is an activated step where the molecule must overcome an energy barrier imposed by the surface potential of the pore walls, followed by gas-state diffusion in a Knudsen-type regime [54]. From our Arrhenius plot, the negative slope of the Arrhenius plot indicates that gas translation separation mechanism dominates the flow [45,50]. However, this is not to say surface diffusion is not present. Membranes often have transport with a combination of surface diffusion and gas translation diffusion [55,56] where the surface diffusion becomes less dominant, or negligible, at higher temperatures, as the adsorption decreases. More highly-adsorbing gases have a higher surface diffusion gas flow [50].

Molecular sieving in many types of graphitic membranes has been observed in the literature, and tends to be described as arising from two main types of structure: (I) in some graphene oxide materials, the sieving is dominated by inter-grain defects and with no apparent major change in permeation characteristics when the interlayer spacing is increased [13], and (II) where sieving is dominated by the interlayer spacing between sheets, whereby smaller molecules can pass between stacked sheets but larger molecules cannot [5,16,47] and thus the larger gases have a much lower permeance. Ibrahim *et al.* [57] recently proposed a two-pathway transport model in graphene oxide, whereby there are inter-sheet pathways composed of nanoscale wrinkles between sheets, and inner-sheet pathways consisting of structural defects in the sheets.

In nanographite, the mechanism shows evidence of being dominated by interlayer spacing, as explained here. We note that neon has a significantly lower permeation, Fig 8, than hydrogen through nanographite membranes, despite being a smaller molecule (0.275 vs 0.289 nm

diameter [49,50]). Similar behaviour has been observed in carbon [5,58] and silica membranes [50,59], where for example, hydrogen has much higher permeance than helium or neon. This behaviour may be explained by the higher relative adsorption of hydrogen compared to neon, which has been measured in porous carbons [60,61] which are comparable to nanographite. Thus at lower temperatures, hydrogen has a larger component of gas-flow which is caused by surface diffusion than neon does. At higher temperatures the adsorption of hydrogen will become less or negligible [60,61] and therefore as the temperature increases, the flow of hydrogen that is caused by surface-diffusion becomes smaller, but this effect is not so strong in neon since the adsorption is relatively small. At higher temperatures, for all gases, any component of transport caused by surface diffusion will become small and the mechanism will turn to pure sized-based molecular sieving, for all gases, which is suggested by the decrease in $\alpha^{H_2}/_{Ne}$ at higher temperatures, Fig. 9.

The higher selectivity of hydrogen over neon further suggests that nanographite has an interlayer sieving mechanism as opposed to inter-grain defect mechanism. Channels formed by interlayer defects tend to have a longer length (~ equal to the crystallite size) than inter-grain defects which tend to be through just one atomic layer [11]. Longer channels provide many adsorption sites, thus allowing significant differential absorption of hydrogen compared to neon, whereas inter-grain defects tend to act solely on size-based sieving [13].

We note that the absolute gas permeance of these membranes is relatively low compared with values found in much of the available literature (Table 2), which is a crucial parameter for membranes to be used in industrial gas separation applications. However, the low permeance of these membranes may largely be explained by the relatively high thickness of these particular samples (350 nm). These were fabricated to this thickness to ensure sufficient strength in order to protect our UHV system from any unintended membrane failure (which we did not observe throughout testing). In other work we have deposited continuous nanographite films of sub-10 nm thickness, for electronic applications [62,63] and this fabrication method for membranes may potentially be carried out on such thin films. If sufficiently robust 10 nm thick membranes could be fabricated, the expected hydrogen permeance would of order $\sim 2 \times 10^{-8}$ mol $\cdot$ m^{-2} $\cdot$ s^{-1} $\cdot$ Pa^{-1} at 150 °C. Further improvements could be made by using nanographite in a mixed-matrix membrane as shown recently in

graphene oxide membranes [64,65] where permeance and mechanical stability was increased by blending graphene oxide with polymer.

The coefficient of permeability C (Equation 4) is a measure of the thickness-normalised permeance, and hence allows better comparison between materials than the absolute permeance. The calculated values of C for hydrogen through nanographite are comparable to related materials such as graphene oxide [13], as detailed in Table 2. Comparing these materials on both permeability and $\alpha^{H_2}/_{CO_2}$ shows that nanographite compares favourably, though we clearly note that further measurement of the absolute permeance of a wider range of gases will be useful. We also include the sieving performance of $\alpha^{He}/_{Ne}$ and $\alpha^{H_2}/_{O_2}$, since these gases are more commonly measured in the literature than $\alpha^{He}/_{Ne}$, for a comparison with a number of other materials. The nanographite membrane consistently shows high separation properties.

Material	Test temp. (°C)	H$_2$ permeance (mol · m^{-2} ·s^{-1} · Pa^{-1})	Sample thickness (μm)	H$_2$ Permeability (mol · m ·m^{-2} · s^{-1} · Pa^{-1})	$\alpha^{H_2}/_{CO_2}$	$\alpha^{He}/_{Ne}$	$\alpha^{H_2}/_{O_2}$
Nanographite [This work]	125	1.53×10^{-10}	0.350	5.35 ×10^{-17}	> 135	48	-
Nanographite [This work]	150	5.11×10^{-10}	0.350	1.79 ×10^{-16}	-	62	>1000
Pressed graphite [5]	150	7.1×10^{-9}	1000	7.1×10^{-12}	~ 4.7	-	-
Graphene-oxide [13]	100	2.0×10^{-7}	0.0018	3.7×10^{-16}	~ 22	-	-
Turbostratic carbon [15]	150	5.7×10^{-9}	~8	4.6×10^{-14}	~ 4.7	-	-
Carbon hollow fiber membranes: [58]	60	1.5×10^{-9}	100	1.5×10^{-13}	8.40	-	55
Silica membranes [66]	200	5.5×10^{-8}	0.2	1.1×10^{-14}	-	10.5	-

Table 2. Summary of the hydrogen permeance and permeation properties and separation between various gases of a number of membranes from the available literature.

4 Conclusions

We have reported for the first time the preparation and permeance testing of freestanding, 350 nm thick, nanographite thin film membranes, produced using PECVD. The method used to fabricate these membranes is scalable and reproducible, using micromachining and deep etching of fused silica wafers. A UHV-based mass spectrometry system is used to measure the permeance of various gases through the membrane and the results show a predominantly gas translation-type permeance behaviour. The gas permeability coefficient of helium and hydrogen is similar to that of related materials such as graphene oxide, however the separation factors of nanographite at elevated temperatures are far higher and in particular,

the separation of $\alpha^{He}/_{Ne}$ equals 48 at 150 °C, $\alpha^{H_2}/_{CO_2}$ >135 at 125 °C and $\alpha^{H_2}/_{O_2}$ >1000 at 150 °C. The high $\alpha^{H_2}/_{CO_2}$, large scale and inexpensive synthesis route, and compatibility for microfabrication show nanographite to be a promising material for micro-scaled membrane applications.

5   <u>Acknowledgements</u>

6   <u>References</u>

[1]   J. Sunarso, S.S. Hashim, Y.S. Lin, S.M. Liu, Membranes for helium recovery: An overview on the context, materials and future directions, Separation and Purification Technology. 176 (2017) 335–383. doi:10.1016/j.seppur.2016.12.020.

[2]   N.W. Ockwig, T.M. Nenoff, Membranes for hydrogen separation, Chemical Reviews. 107 (2007) 4078–4110. doi:10.1021/cr0501792.

[3]   Z. Cai, R.H. Clarke, B.A. Glowacki, W.J. Nuttall, N. Ward, Ongoing ascent to the helium production plateau-Insights from system dynamics, Resources Policy. 35 (2010) 77–89. doi:10.1016/j.resourpol.2009.10.002.

[4]   W.J. Nuttall, R.H. Clarke, B.A. Glowacki, Resources: Stop squandering helium, Nature. 485 (2012) 573–575. doi:10.1038/485573a.

[5]   A. Schulz, F. Steinbach, J. Caro, Pressed graphite crystals as gas separation membrane for steam reforming of ethanol, Journal of Membrane Science. 469 (2014) 284–291. doi:10.1016/j.memsci.2014.06.047.

[6]   C. Huang, H. Wu, K. Deng, W. Tang, E. Kan, Improved permeability and selectivity in porous graphene for hydrogen purification, Phys. Chem. Chem. Phys. 16 (2014) 25755–25759. doi:10.1039/C4CP04385E.

[7]   J. Schrier, Helium separation using porous graphene membranes, Journal of Physical

Chemistry Letters. 1 (2010) 2284–2287. doi:10.1021/jz100748x.

[8] M. Bartolomei, E. Carmona-Novillo, M.I. Hernández, J. Campos-Martínez, F. Pirani, G. Giorgi, Graphdiyne pores: Ad hoc openings for helium separation applications, Journal of Physical Chemistry C. 118 (2014) 29966–29972. doi:10.1021/jp510124e.

[9] F. Li, Y. Qu, M. Zhao, Efficient helium separation of graphitic carbon nitride membrane, Carbon. 95 (2015) 51–57. doi:10.1016/j.carbon.2015.08.013.

[10] W. Hu, X. Wu, Z. Li, J. Yang, Helium separation via porous silicene based ultimate membrane, Nanoscale. 5 (2013) 9062–9066. doi:10.1039/C3NR02326E.

[11] M.S.H. Boutilier, C. Sun, S.C. O'Hern, H. Au, N.G. Hadjiconstantinou, R. Karnik, Implications of permeation through intrinsic defects in graphene on the design of defect-tolerant membranes for gas separation, ACS Nano. 8 (2014) 841–849. doi:10.1021/nn405537u.

[12] H.W. Kim, H.W. Yoon, S. Yoon, B.M. Yoo, B.K. Ahn, Y.H. Cho, et al., Selective Gas Transport Through few-layered graphene and graphene oxide membranes, Science. 342 (2013) 91–95. doi:10.1126/science.1236098.

[13] H. Li, Z. Song, X. Zhang, Y. Huang, S. Li, Y. Mao, et al., Ultrathin, Molecular-Sieving Graphene Oxide Membranes for Selective Hydrogen Separation, Science. 342 (2013) 95–98. doi:10.1126/science.1236686.

[14] C. Chi, X. Wang, Y. Peng, Y. Qian, Z. Hu, J. Dong, et al., Facile Preparation of Graphene Oxide Membranes for Gas Separation, Chemistry of Materials. 28 (2016) 2921–2927. doi:10.1021/acs.chemmater.5b04475.

[15] A. Wollbrink, K. Volgmann, J. Koch, K. Kanthasamy, C. Tegenkamp, Y. Li, H. Richter, et al., Amorphous, turbostratic and crystalline carbon membranes with hydrogen selectivity, Carbon. 106 (2016). doi:http://dx.doi.org/10.1016/j.carbon.2016.04.062.

[16] E.A. Efimova, D.A. Syrtsova, V. V. Teplyakov, Gas permeability through graphite foil: The influence of physical density, membrane orientation and temperature, Separation and Purification Technology. 179 (2017) 467–474. doi:10.1016/j.seppur.2017.02.023.

[17] Y. Yang, P. Dementyev, N. Biere, D. Emmrich, P. Stohmann, R. Korzetz, et al., D. Anselmetti, Rapid Water Permeation Through Carbon Nanomembranes with Sub-Nanometer Channels, ACS Nano. Article (2018). doi:10.1021/acsnano.8b01266.

[18] J.B.S. Hamm, A.R. Muniz, L.D. Pollo, N.R. Marcilio, I.C. Tessaro, Experimental and computational analysis of carbon molecular sieve membrane formation upon

polyetherimide pyrolysis, Carbon. 119 (2017) 21–29. doi:10.1016/j.carbon.2017.04.011.

[19] M.J. Varady, L. McLeod, J.M. Meacham, F.L. Degertekin, A.G. Fedorov, An integrated MEMS infrastructure for fuel processing: Hydrogen generation and separation for portable power generation, Journal of Micromechanics and Microengineering. 17 (2007). doi:10.1088/0960-1317/17/9/S08.

[20] T. Boeltken, A. Wunsch, T. Gietzelt, P. Pfeifer, R. Dittmeyer, Ultra-compact microstructured methane steam reformer with integrated Palladium membrane for on-site production of pure hydrogen: Experimental demonstration, International Journal of Hydrogen Energy. 39 (2014) 18058–18068. doi:10.1016/j.ijhydene.2014.06.091.

[21] B.A. Wilhite, S.E. Weiss, J.Y. Ying, M.A. Schmidt, K.F. Jensen, High-purity hydrogen generation in a microfabricated 23 wt % Ag-Pd membrane device integrated with 8:1 $LaNi_{0.95}Co_{0.05}O_3/Al_2O_3$ catalyst, Advanced Materials. 18 (2006) 1701–1704. doi:10.1002/adma.200502025.

[22] H. Medina, Y.-C.C. Lin, C.H. Jin, C.-C.C. Lu, C.-H.H. Yeh, K.-P.P. Huang, et al., Metal-Free Growth of Nanographene on Silicon Oxides for Transparent Conducting Applications, Advanced Functional Materials. 22 (2012) 2123–2128. doi:10.1002/adfm.201102423.

[23] L. Zhang, Z. Shi, Y. Wang, R. Yang, D. Shi, G. Zhang, Catalyst-free growth of nanographene films on various substrates, Nano Research. 4 (2010) 315–321. doi:10.1007/s12274-010-0086-5.

[24] M.E. Schmidt, C. Xu, M. Cooke, H. Mizuta, H.M.H. Chong, Metal-free plasma-enhanced chemical vapor deposition of large area nanocrystalline graphene, Materials Research Express. 1 (2014) 025031. doi:10.1088/2053-1591/1/2/025031.

[25] S.J. Fishlock, D. Grech, J.W. McBride, H.M.H. Chong, S.H. Pu, Mechanical characterisation of nanocrystalline graphite using micromechanical structures, Microelectronic Engineering. 159 (2016) 184–189. doi:10.1016/j.mee.2016.03.040.

[26] S.J. Fishlock, S.J. O'Shea, J.W. McBride, H.M.H. Chong, S.H. Pu, Fabrication and characterisation of nanocrystalline graphite MEMS resonators using a geometric design to control buckling, Journal of Micromechanics and Microengineering. 27 (2017). doi:10.1088/1361-6439/aa7ebb.

[27] J.-Y. Jin, S. Yoo, J.-S. Bae, Y.-K. Kim, Deep wet etching of borosilicate glass and fused silica with dehydrated AZ4330 and a Cr/Au mask, Journal of Micromechanics and Microengineering. 24 (2014) 015003. doi:10.1088/0960-1317/24/1/015003.

21

[28] P. Tremblay, M. Savard, J. Vermette, R. Paquin, Gas permeability, diffusivity and solubility of nitrogen, helium, methane, carbon dioxide and formaldehyde in dense polymeric membranes using a new on-line permeation apparatus, Journal of Membrane Science. 282 (2006) 245–256. doi:10.1016/j.memsci.2006.05.030.

[29] G. Firpo, E. Angeli, L. Repetto, U. Valbusa, Permeability thickness dependence of polydimethylsiloxane (PDMS) membranes, Journal of Membrane Science. 481 (2015) 1–8. doi:10.1016/j.memsci.2014.12.043.

[30] O.B. Malyshev, K.J. Middleman, In situ ultrahigh vacuum residual gas analyzer "calibration," Journal of Vacuum Science & Technology A. 26 (2008) 1474–1479. doi:10.1116/1.2990856.

[31] C.D. Ehrlich, J.A. Basford, Recommended practices for the calibration and use of leaks, Journal of Vacuum Science & Technology A. 10 (1992) 1–17. doi:10.1116/1.578137.

[32] Y. Ishikawa, T. Yoshimura, Importance of the surface oxide layer in the reduction of outgassing from stainless steels, Journal of Vacuum Science & Technology A. 13 (1995) 1847–1852. doi:10.1116/1.579669.

[33] Y. Li, F. Liang, H. Bux, W. Yang, J. Caro, Zeolitic imidazolate framework ZIF-7 based molecular sieve membrane for hydrogen separation, Journal of Membrane Science. 354 (2010) 48–54. doi:10.1016/j.memsci.2010.02.074.

[34] Table of units, Journal of Membrane Science. 366 (2011) III–III. doi:10.1016/S0376-7388(10)00894-X.

[35] W. Yang, C. He, L. Zhang, Y. Wang, Z. Shi, M. Cheng, et al., Growth, characterization, and properties of nanographene., Small. 8 (2012) 1429–35. doi:10.1002/smll.201101827.

[36] J. Sun, M.E. Schmidt, M. Muruganathan, H.M.H. Chong, H. Mizuta, Large-scale nanoelectromechanical switches based on directly deposited nanocrystalline graphene on insulating substrates, Nanoscale. 8 (2016) 6659–6665. doi:10.1039/C6NR00253F.

[37] A.C. Ferrari, J. Robertson, Interpretation of Raman spectra of disordered and amorphous carbon, Physical Review B. 61 (2000) 14095–14107. doi:10.1103/PhysRevB.61.14095.

[38] T.M.G. Mohiuddin, A. Lombardo, R.R. Nair, A. Bonetti, G. Savini, R. Jalil, et al., Uniaxial strain in graphene by Raman spectroscopy: G peak splitting, Grüneisen parameters, and sample orientation, Physical Review B. 79 (2009) 205433. doi:10.1103/PhysRevB.79.205433.

[39] E.H. Martins Ferreira, M.V.O. Moutinho, F. Stavale, M.M. Lucchese, R.B. Capaz, C.A. Achete, et al., Evolution of the Raman spectra from single-, few-, and many-layer graphene with increasing disorder, Physical Review B - Condensed Matter and Materials Physics. 82 (2010). doi:10.1103/PhysRevB.82.125429.

[40] Q. Nian, Y. Wang, Y. Yang, J. Li, M.Y. Zhang, J. Shao, et al., Direct laser writing of nanodiamond films from graphite under ambient conditions, Scientific Reports. 4 (2014) 1–8. doi:10.1038/srep06612.

[41] B.D. Cullity, Elements of X-ray Diffraction, Third Edition, Prentice-Hall, New York, USA, 2001.

[42] N.J. Hargreaves, S.J. Cooper, Nanographite Synthesized from Acidified Sucrose Microemulsions under Ambient Conditions, Crystal Growth and Design. 16 (2016) 3133–3142. doi:10.1021/acs.cgd.5b01753.

[43] A.L. Patterson, The Scherrer formula for X-ray particle size determination, Physical Review. 56 (1939) 978. doi:10.1103/PhysRev.56.978.

[44] V.Y. Osipov, T. Enoki, K. Takai, K. Takahara, M. Endo, T. Hayashi, et al., Magnetic and high resolution TEM studies of nanographite derived from nanodiamond, Carbon. 44 (2006) 1225–1234. doi:10.1016/j.carbon.2005.10.047.

[45] J. Gilron, A. Soffer, Knudsen diffusion in microporous carbon membranes with molecular sieving character, Journal of Membrane Science. 209 (2002) 339–352. doi:10.1016/S0376-7388(02)00074-1.

[46] R.S.A. De Lange, K. Keizer, A.J.J. Burggraaf, R.S.A. de Lange, K. Keizer, A.J.J. Burggraaf, Analysis and theory of gas transport in microporous sol-gel derived ceramic membranes, Journal of Membrane Science. 104 (1995) 81–100. doi:10.1016/0376-7388(95)00014-4.

[47] J. Shen, G. Liu, K. Huang, W. Jin, K.R. Lee, N. Xu, Membranes with fast and selective gas-transport channels of laminar graphene oxide for efficient CO_2 capture, Angewandte Chemie - International Edition. 54 (2015) 578–582. doi:10.1002/anie.201409563.

[48] C.P. Herrero, R. Ramírez, Diffusion of hydrogen in graphite: A molecular dynamics simulation, Journal of Physics D: Applied Physics. 43 (2010). doi:10.1088/0022-3727/43/25/255402.

[49] H.L. Castricum, H.F. Qureshi, A. Nijmeijer, L. Winnubst, Hybrid silica membranes with enhanced hydrogen and CO_2 separation properties, Journal of Membrane Science. 488 (2015) 121–128. doi:10.1016/j.memsci.2015.03.084.

23

[50] W.J.W. Bakker, L.J.P. Van Den Broeke, F. Kapteijn, J.A. Moulijn, Temperature dependence of one-component permeation through a silicalite-1 membrane, AIChE Journal. 43 (1997) 2203–2214. doi:10.1002/aic.690430907.

[51] W.J. Koros, G.K. Fleming, Membrane-based gas separation, Journal of Membrane Science. 83 (1993) 1–80. doi:10.1016/0376-7388(93)80013-N.

[52] P. Pandey, R.S. Chauhan, Membranes for gas separation, Progress in Polymer Science. 26 (2001) 853–893. doi:10.1016/S0079-6700(01)00009-0.

[53] A.W. Thornton, A. Ahmed, S.K. Kannam, B.D. Todd, M. Majumder, A.J. Hill, Analytical Diffusion Mechanism (ADiM) model combining specular, Knudsen and surface diffusion, Journal of Membrane Science. 485 (2015) 1–9. doi:10.1016/j.memsci.2015.03.004.

[54] S.B. Messaoud, A. Takagaki, T. Sugawara, R. Kikuchi, S.T. Oyama, Alkylamine-silica hybrid membranes for carbon dioxide/methane separation, Journal of Membrane Science. 477 (2015) 161–171. doi:10.1016/j.memsci.2014.12.022.

[55] J.C. Poshusta, R.D. Noble, J.L. Falconer, Temperature and pressure effects on CO_2 and CH_4 permeation through MFI zeolite membranes, Journal of Membrane Science. 160 (1999) 115–125. doi:10.1016/S0376-7388(99)00073-3.

[56] P.F. Zito, A. Caravella, A. Brunetti, E. Drioli, G. Barbieri, Knudsen and surface diffusion competing for gas permeation inside silicalite membranes, Journal of Membrane Science. 523 (2017) 456–469. doi:10.1016/j.memsci.2016.10.016.

[57] A. Ibrahim, Y.S. Lin, Gas permeation and separation properties of large-sheet stacked graphene oxide membranes, Journal of Membrane Science. 550 (2018) 238–245. doi:10.1016/j.memsci.2017.12.081.

[58] E.P. Favvas, N.S. Heliopoulos, S.K. Papageorgiou, A.C. Mitropoulos, G.C. Kapantaidakis, N.K. Kanellopoulos, Helium and hydrogen selective carbon hollow fiber membranes: The effect of pyrolysis isothermal time, Separation and Purification Technology. 142 (2015) 176–181. doi:10.1016/j.seppur.2014.12.048.

[59] S.T. Oyama, D. Lee, P. Hacarlioglu, R.F. Saraf, Theory of hydrogen permeability in nonporous silica membranes, Journal of Membrane Science. 244 (2004) 45–53. doi:10.1016/j.memsci.2004.06.046.

[60] R.M. Barrer, E. Strachan, Sorption and Surface Diffusion in Microporous Carbon Cylinders, Proceedings of the Royal Society of London A: Mathematical, Physical and Engineering Sciences. 231 (1955) 52–74. doi:10.1098/rspa.1955.0156.

[61] C.K. Chan, E. Tward, K.I. Boudaie, Adsorption isotherms and heats of adsorption of

hydrogen, neon and nitrogen on activated charcoal, Cryogenics. 24 (1984) 451–459. doi:10.1016/0011-2275(84)90001-8.

[62] T.Y. Ling, S.J. Fishlock, M.S. Shamsudin, S.M. Sultan, H.M.H. Chong, S.H. Pu, Design and fabrication of a nanocrystalline graphite thin-film sensor for in situ ionic concentration monitoring, in: Proceedings of IEEE Sensors, 2017. doi:10.1109/ICSENS.2017.8234336.

[63] S.M. Sultan, S.H. Pu, S.J. Fishlock, L.H. Wah, H.M.H. Chong, J.W. McBride, Electrical behavior of nanocrystalline graphite/p-Si Schottky diode, in: 2016 IEEE 16th International Conference on Nanotechnology (IEEE-NANO), 2016: pp. 307–310. doi:10.1109/NANO.2016.7751379.

[64] Z. Wang, H. Yu, J. Xia, F. Zhang, F. Li, Y. Xia, et al., Novel GO-blended PVDF ultrafiltration membranes, Desalination. 299 (2012) 50–54. doi:10.1016/j.desal.2012.05.015.

[65] S. Castarlenas, C. Téllez, J. Coronas, Gas separation with mixed matrix membranes obtained from MOF UiO-66-graphite oxide hybrids, Journal of Membrane Science. 526 (2017) 205–211. doi:10.1016/j.memsci.2016.12.041.

[66] S.J. Ahn, G.N. Yun, A. Takagaki, R. Kikuchi, S.T. Oyama, Synthesis and characterization of hydrogen selective silica membranes prepared by chemical vapor deposition of vinyltriethoxysilane, Journal of Membrane Science. 550 (2018) 1–8. doi:10.1016/j.memsci.2017.12.038.

1 **Micromachined nanocrystalline graphite membranes for gas separation**

2

3 S.J. Fishlock[1-5*], S.H. Pu[1,3,4], G. Bhattacharya[5,6], Yisong Han[5], J. McLaughlin[5],

4 J.W. McBride[1,3], H.M.H. Chong[4] and S.J. O'Shea[2].

5 [1]Mechatronics Research Group, Faculty of Engineering and the Environment, University of

6 Southampton, Southampton SO17 1BJ, UK

7 [2] A*STAR, Institute of Materials Research and Engineering (IMRE) 2 Fusionopolis Way,

8 Innovis, Singapore, 138634

9 [3]University of Southampton Malaysia Campus, Iskandar Puteri, 79200, Johor, Malaysia

10 [4]Sustainable Electronic Technologies Research Group, School of Electronics and Computer

11 Science, University of Southampton, Southampton SO17 1BJ, UK

12 [5]Nanotechnology Integrated Bio-Engineering Centre, University of Ulster, Shore Road,

13 BT37 0QB Newtownabbey, United Kingdom

14 [6]Department of Physics, School of Natural Sciences, Shiv Nadar University, Gautam Buddha

15 Nagar 201314, Uttar Pradesh, India.

16 **Abstract**

17 Carbon nanoporous membranes show promising performance for the passive separation and

18 sieving of different gases, for example for helium and hydrogen separation. In this paper,

19 nanocrystalline graphite (or nanographite) has been evaluated as a membrane material for

20 molecular sieving of helium and hydrogen from larger gas constituents. Nanographite of 350

21 nm thickness was prepared using plasma-enhanced chemical vapour deposition onto fused

22 silica substrates, from which membranes were microfabricated using deep wet etching.

23 Permeability of Hydrogen and Helium were 1.79×10^{-16} and 1.40×10^{-16} mol·m·m^{-2}·s^{-1}·Pa^{-1} at

24 150 °C respectively, and measured separation was 48 for He/Ne, >135 for H_2/CO_2 and >1000

25 for H_2/O_2. The gas separation properties of the nanographite membranes were tested in the

26 temperature range of 25 to 150 °C, and the permeation measurements show nanographite to be

27 highly selective of helium and hydrogen over all larger gas molecules, including neon.

28

29 *Corresponding author. Tel +442890368433. E-mail s.fishlock@ulster.ac.uk (Sam Fishlock)

30

1   **1. <u>Introduction</u>**

2   Nanoporous membranes are attractive candidates for use as molecular sieves for the separation

3   of helium and hydrogen from the larger constituents of natural gas [1,2]. Helium is an

4   irreplaceable natural resource which is widely used in many industrial and scientific

5   applications such as cryogenics and CMOS fabrication [1]. Helium is commonly extracted

6   from fields of natural gas using cryogenic processing, whereby the mixture of gases is separated

7   cryogenically [3]. This highly energy intensive process is often not financially viable and in

8   many cases the helium is permanently lost to atmosphere [4], and as a result, less energy-

9   intensive methods of helium extraction are sought, and molecular sieving using membranes is

10   considered a promising method of production. Similarly, hydrogen is an important fuel and is

11   also generally obtained from, for example, natural gas and bioethanol, which leaves hydrogen

12   in a mixture of undesired products such as CO_2, CH_4 and CO which need to be further

13   separated [5,6].

14

15   Several theoretical studies have shown the promise of 2D materials such as graphene [7],

16   graphdiyne [8], carbon nitride [9] and silicene [10] to be used as molecular sieves for helium

17   and hydrogen separation. These simulations show that the intrinsic pores in 2D materials

18   caused by vacancies such as Stone-Wales defects and pores could enable membranes with very

19   high flux of helium or hydrogen, combined with high separation from all other gases [7].

20   However, the prospect of fabricating robust, temperature resistant, large-area 2D films, with

21   the presence of solely specific and 'tailored' defects (as opposed to non-specific defects and

22   pores) remains somewhat distant. For example, studies of the gas transport through stacked

23   graphene sheets have shown that tears and unintended defects greatly reduce the sieving

24   properties of membranes [11].

25

26   As a result of the potential challenges facing the upscaling of 'pure' 2D thin films, related

27   porous materials such as thin graphite oxide or graphene oxide [12,13] are considered to be

28   promising molecular sieve materials, as this has more scalable and reproducible production,

29   and is more viable to be used in large-scale applications. However the behaviour of graphene

30   oxide molecular sieves currently show a small window of operation regarding temperature;

31   with the separation factor of H_2 and CO_2 ($\alpha^{H_2}/_{CO_2}$) for 1.8 nm thick membranes, falling from ~

32   2090 at 20 °C to ~ 22 at 100 °C [13]. A similar result was observed in graphene oxide

33   membranes by Chi *et al.* with $\alpha^{H_2}/_{CO_2}$ falling from 240 at room temperature to 47 at 120 °C

2

1 [14]. As a result, a wider range of carbon materials are sought as molecular sieves due to their

2 high flux and temperature resistance [2]. Recent studies on carbon materials have included

3 pressed graphite [5] turbostratic and amorphous carbon [15], graphite foils [16], carbon

4 nanomembranes derived from terphenylthiol [17] and polymer-derived carbons [18].

5

6 Furthermore, micromachined and miniaturised membranes for hydrogen separation are of

7 specific interest in the use of micro-generators based on hydrogen production in micro-reactors

8 [19–21]. In such systems, hydrogen is produced from steam reforming of methane [20] or

9 catalytic reaction from methanol [21]. This chip-scaled power enables a high-density and high

10 efficiency power source, which is required in certain aerospace [19] and consumer electronics

11 [21] applications. High purification and separation of hydrogen from larger gas constituents

12 are required to help bring such micro-reactor generators to wider use. Currently, such micro-

13 reactors have typically relied on hydrogen separation using palladium membranes [19–21]

14 which are highly expensive, and suffer excessive sensitivity to surface contamination [2].

15

16 In this study, we explore the use of thin-film nanocrystalline graphite (referred to as NCG,

17 nanographene or nanographite) micro-scaled membranes, as a candidate material for helium

18 and hydrogen separation. Nanographite has crystallite sizes of roughly ~ 2 to 50 nm [22–24].

19 One advantage of nanographite is that it may be deposited onto large-area substrates using

20 plasma-enhanced chemical vapour deposition (PECVD) without any metal catalyst; this

21 enables fabrication and characterisation of freestanding membranes using MEMS-type

22 technology such as lithographic patterning and etching. Here, we demonstrate a method to

23 fabricate freestanding thin-film membranes using deep HF etching which may be used for batch

24 production of micro-scaled membranes. We present the gas permeation and separation

25 behaviour of nanographite membranes in the temperature range of 25 to 150 °C, and

26 demonstrate this to be a promising membrane material with high sieving behaviour,

27 inexpensive, large area synthesis and preparation, and potential for micro-scaled applications.

28

1 **2. Experimental**

2   2.1 Deposition of nanographite

3 Nanographite was deposited onto a 4-inch fused silica wafer (University Wafers, USA), using

4 a commercial PECVD tool (Oxford Instruments Nanofab1000 Agile), with a CH_4 precursor

5 and H_2 diluent at a temperature of 750 °C. The further deposition conditions, and detailed

6 mechanical characterisation have been described in previous work by our group [24–26].

7   2.2 Material characterisation

8 Raman spectroscopy (Renishaw inVia) was used to characterise the structural properties of the

9 nanographite film, using a 532 nm wavelength excitation laser and $50 \times$ magnification.

10 Scanning electron microscopy (JEOL JSM 6700F, 5.0 kV accelerating voltage) was used to

11 view the morphology of the film on the as-deposited fused silica substrate. Grazing angle X-

12 ray diffraction was performed (Bruker D8) using a CuK_α source with wavelength of 0.154 nm.

13 TEM samples were prepared using mechanical exfoliation into ethanol, sonicated for 10

14 minutes and micropipetted onto copper-supported holey carbon grids (Agar Scientific Holey

15 carbon film on 300 mesh cu). HRTEM (JEOL JEM-2100F) was used for imaging at 200 keV

16 excitation.

17   2.3   Microfabrication of membranes

18 To fabricate a membrane, nanographite was deposited to a thickness of 350 nm onto one side

19 of a doubly-polished 4-inch fused silica wafer. The nanographite was annealed at a temperature

20 of 1000 °C for one minute under N_2 flow, after vacuum evacuation, using a rapid thermal

21 annealer (Jipelec JetFirst 150) to reduce the compressive stress of the film. Without the

22 annealing step, a high level of buckling and breakage was observed. A chrome/gold (10/300 nm

23 thickness) mask was patterned on the wafer back side using thermal evaporation (Fig. 1 (A)),

24 over which a 7 μm layer of AZ4330 resist was spun, and patterned with a circular window of

25 25 μm diameter, Fig. 1 (B). The wafer was then post-baked for 20 minutes at 120 °C in an

26 oven. This post-bake was used to make the resist layer more hydrophobic [27] and thus reduce

27 pinhole damage to the gold mask from the later deep hydrofluoric acid (HF) etch.   The

28 chrome/gold mask was etched using Aldrich gold etchant and Microchrome Technology, CEP-

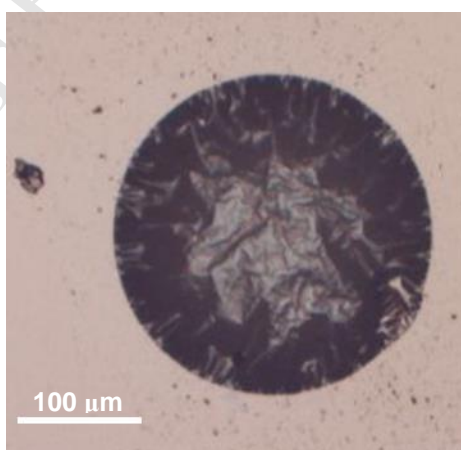29 200 chrome etchant respectively.

30

31 The wafer was then diced and the front side of each membrane chip was protected from the HF

32 by adhering the surface to a silicon wafer using melted wax, heated at 50 °C and then left to

1 cool at room temperature. 49 % HF acid was used to isotropically etch the fused silica through
2 to the nanographite, thus releasing the membrane, Fig. 1 (C). The etching process typically
3 took around 12 to 16 hours. After etching, the wax was melted and the chip thoroughly cleaned
4 in, successively, acetone, deionised water and isopropyl alcohol, Fig. 1 (D). A microscope
5 image of a released membrane is shown in Fig. 2. The membrane is slightly buckled due to
6 some remaining compressive stress, but remained fairly robust. This fabrication process gave
7 reproducible results, with around 75 % of 100 – 1000 μm diameter membranes successfully
8 released.

9
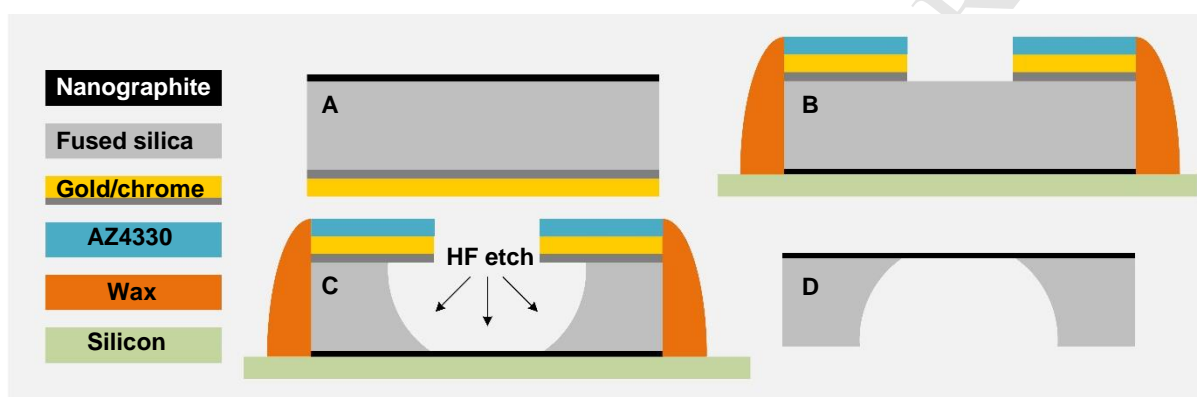
10

11 Fig. 1. Schematic fabrication process of nanographite membranes on fused silica substrates.
12 (A) Deposition of nanographite using PECVD and Cr/Au using thermal evaporation. (B)
13 Photolithography using AZ4330 resist followed by Au and Cr etching, front protection using
14 wax and a silicon carrier. (C) Deep HF etching. (D) Wax melting and solvent cleaning.

15

16

17 Fig. 2. Microscope image of a released nanographite membrane taken from the top side. The
18 membrane shows slight crumpling due to some compressive stress.

5

1   2.4   Mass spectrometry system for permeance measurement

2 The flux of gases through the membrane was calculated by measuring the downstream pressure

3 of gas using a residual gas analyser (RGA, SRS RGA 300) type quadrupole mass spectrometer

4 in an ultra-high vacuum (UHV) chamber. Fig. 3 shows a schematic of the system, and is similar

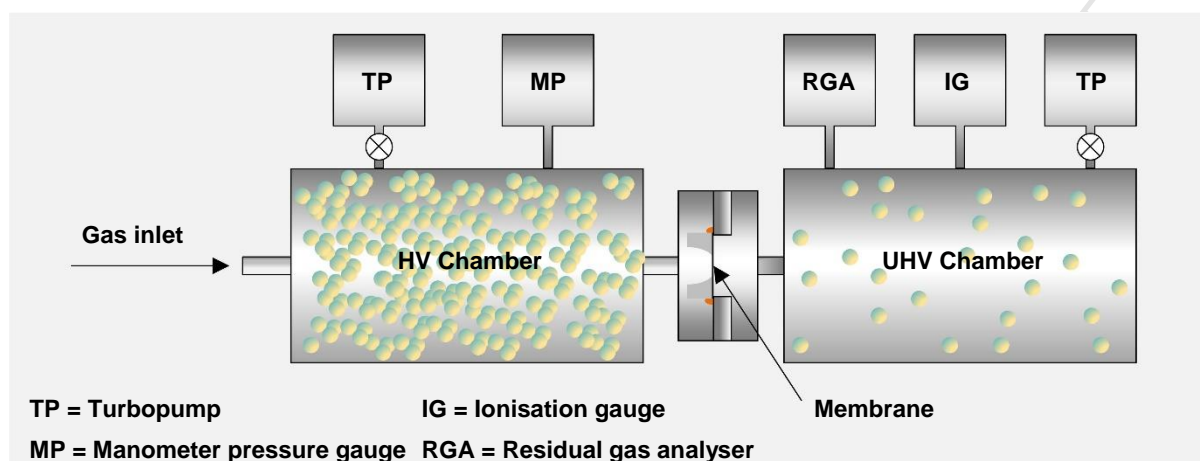5 to permeation testing rigs used in other reports [28,29].

6

7 Fig. 3. Schematic of UHV rig used to measure the permeance of nanographite membranes.

8

9 The rig comprises two chambers, separated by the membrane. The larger chamber (6.74 L

10 volume) is at ultrahigh vacuum (UHV) in which sensitive gas partial pressure measurements

11 are made using the RGA, and a smaller chamber evacuated to high vacuum (HV), which during

12 testing is filled with the analyte gas to a pressure up to 80 Torr. The membrane was sealed over

13 a 1/4'' stainless steel Swagelok gasket using a UHV-rated 2-part adhesive (Allectra 330s-

14 GLUE1-M3). The gasket was then adhered using the same adhesive over the orifice connecting

15 the two chambers. The UHV chamber was evacuated using a Varian V-551 turbomolecular

16 pump rated to 550 L s^{-1}. The system was thoroughly baked overnight using external heater

17 tapes at 150 °C to remove water vapour and other contaminants from the system walls. After

18 baking, a UHV base pressure of around 1×10^{-10} Torr was achieved. The two chambers are

19 separated by the membrane, and gas flows through due to the concentration gradient. To

20 measure the flux through the membrane, the UHV chamber was shut off from the evacuating

21 turbopump and the pressure rise of the analyte gas was measured until the overall pressure in

22 the UHV chamber reached around 1×10^{-5} Torr. During measurement, only the pressure of the

23 analyte gas was measured, as the RGA enables measurement of the ion current at a specified

24 atomic mass, whilst ignoring the pressure of other background gases. The RGA was calibrated

25 against a total-pressure ionisation gauge [30].

1

2 To test the leak-tightness of the membrane holder, a blank (plain fused silica chip) was adhered

3 over a gasket, and helium was flowed to a pressure of 80 Torr to the HV side of the setup and

4 the pressure observed using the RGA. No pressure rise of helium was observed, showing that

5 during testing all flowing gas should be through the membrane itself. To measure the flux of

6 gases through the membrane at elevated temperature, the membrane holder and adjacent

7 components were wrapped in heating tape and aluminium foil, to help maintain homogenous

8 heating throughout. A thermocouple was taped to the outer face of the membrane holder using

9 conductive carbon tape and the sample was heated and maintained at temperature for one hour

10 prior to permeation measurement. The measurement of helium, hydrogen, neon, oxygen and

11 carbon dioxide was performed through a nanographite membrane at temperatures from room

12 temperature (25 °C) to 150 °C.

13 ### 2.5   Gas flux measurement

14 The membrane leak rate Q_m (Pa $\cdot$ m^3 $\cdot$ s^{-1}) can be calculated by measuring the change in partial

15 pressure of the analyte gas with time, as described in Equation 1 [31]:

16 $$Q_m = \left[\left(\Delta P_{avg} / \Delta t \right) - \left(\Delta P_0 / \Delta t \right) \right] \cdot v \qquad (1)$$

17 where ΔP_{avg} is the measured change in pressure over a time period Δt, ΔP_0 is the measured

18 change in background pressure arising from gases emanating from the vacuum chamber

19 internal surfaces and v is the measured volume of the chamber. This pressure rise occurs in the

20 UHV system, when the turbopump valve has been closed, to allow the analyte gas pressure to

21 build up. ΔP_0 was measured from the background signal, by measuring the pressure rise when

22 there was no analyte gas present in the HV chamber. ΔP_0 was negligible in the case of helium,

23 since there is no ambient helium present in the UHV chamber, however ΔP_0 was non-negligible

24 in the case of hydrogen, since some hydrogen diffuses from the inner steel walls of the UHV

25 chamber, particularly from the grain boundaries [32]. From the leak rate, the molar flux, J,

26 (mol m^{-2}s^{-1}) may be calculated by [31]:

27 $$J = Q_m / RTa \qquad (2)$$

28 where a is the geometric surface area of the membrane, R is the molar gas constant and T is the

29 absolute temperature. The permeance, B, (mol $\cdot$ m^{-2} $\cdot$ s^{-1} $\cdot$ Pa^{-1}) is defined as [33]:

30 $$B = J / P_{hv} \qquad (3)$$

1   where P_{hv} is the upstream pressure of the gas, in the HV chamber. The coefficient of

2   permeability C (mol · m ·m^{-2} · s^{-1} · Pa^{-1}) is a measure of the thickness-normalised permeance

3   of a membrane material [34] and is calculated as:

4 $$C = B \cdot x \tag{4}$$

5   where x is the membrane thickness. The selectivity α of two gases is calculated as the ratio of

6   the permeance of both gases, flowing under the same conditions:

7 $$\alpha = \frac{B_1}{B_2} \tag{5}$$

8   **3**   **Results and discussion**

9   3.1 Material characterisation

10 Nanocrystalline graphite comprises nano-scaled crystallites of sp^2 bonded carbon [35,36]. A

11 Raman spectrum obtained from a nanographite thin film is shown in Fig. 4, with the main peaks

12 highlighted. The characteristic D peak (A_{1g} breathing mode 1350 cm^{-1}) arises from defects such

13 as grain boundaries and dislocations in the graphitic structure, and is characteristic of defected

14 graphene or graphite [37] and the G peak (E_{2g} mode 1594 cm^{-1}) is the so-called 'graphite mode'

15 and originates from the radial breathing mode of sp^2 carbon [37]. The 2D peak (second order

16 of the D peak of 2690 cm^{-1}) is an overtone of the D peak [38]. The G+D' peak (1594 cm^{-1}) is

17 defect related [39]. To calculate I_D/I_G we fit Lorentzian peaks (Origin Pro 9.3) to the D and G

18 peaks, with a Fano peak for the slight shoulder of D' (1620 cm^{-1}) [24,39] and I_D/I_G equals

19 ~1.79 which is characteristic of a nanocrystalline graphite [37]. An SEM image of nanographite

20 is included in Fig. 5, which shows the granular structure of nanographite.
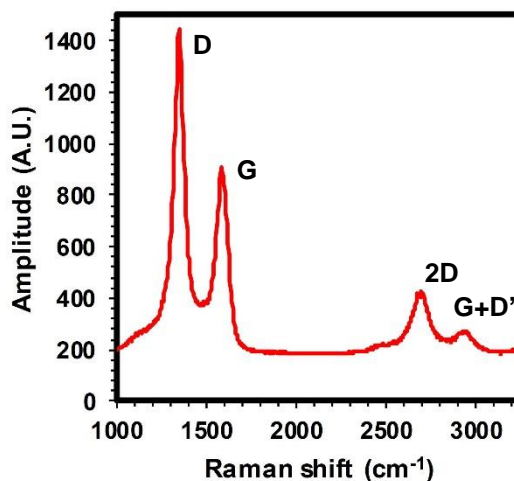
1   Fig. 4. Raman spectrum of 350 nm thick nanographite sample, on a fused silica substrate with

2   the main peaks denoted.

3
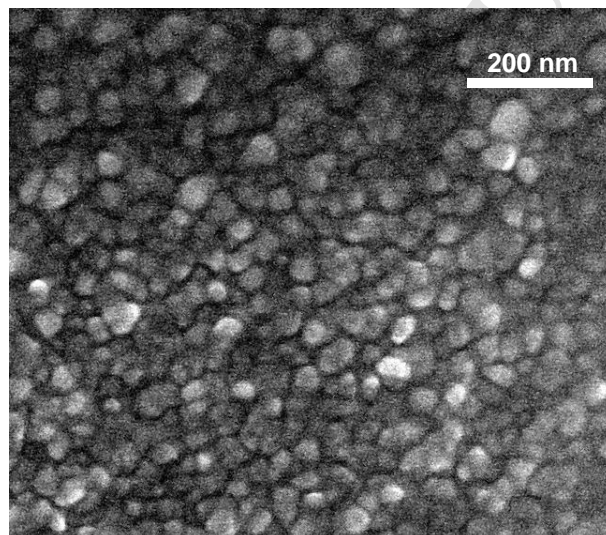
4

5   Fig. 5. SEM image of nanographite morphology on fused silica substrate.

6

7   X-ray diffraction (XRD) was carried out to confirm the presence of graphitic phases. The XRD

8   pattern of nanocrystalline graphite deposited on fused silica substrate is shown in Fig. 6. The

9   plot mainly consists of two broad peaks centered at $2\theta \sim 21.8^{\circ}$ and $2\theta \sim 43.7^{\circ}$. The first peak

10   can be attributed to the fused silica substrate, as observed previously [40]. In order to confirm

11   that the peak arises because of the substrate, a similar grazing angle XRD was also carried out

12   on the pristine substrate, shown in Fig. 6, and a similar peak is obtained. The second XRD peak

13   around $2\theta \sim 43.7^{\circ}$ can be assigned to the graphite (100) crystal plane [40] with some inherent

14   strain. In order to calculate the hexagonal spacing we used Bragg's equation [41]:

9

$$2d \sin \theta = n\lambda \qquad (6)$$

where θ is half of the diffraction angle, n equals 1 and λ is the wavelength of X-rays (0.154 nm). The hexagonal spacing (d_{100}) is calculated as ~0.21 nm which corresponds closely to similar studies on nanographite [42]. Because of the lack of long range crystallinity of the nanographite, a very high fullwidth at half maximum (FWHM) (~0.05 radian) is obtained. The crystallite size was further calculated using the Scherrer equation [43]:

$$D = \frac{k\lambda}{\beta \cos \theta} \qquad (7)$$

where D is the average crystalline size, k is a constant (k=0.89), λ is the wavelength of X-rays (0.154 nm), β is the FWHM of the diffraction peak and θ is half of the diffraction angle. The average crystalline size is calculated, and the value of D is found to be ~ 3.0 nm, which is similar to the crystallite size measured by Hargreaves *et al.* [42] who measured a mean graphene domain size of ~ 1 - 3 nm, with some larger crystallites.
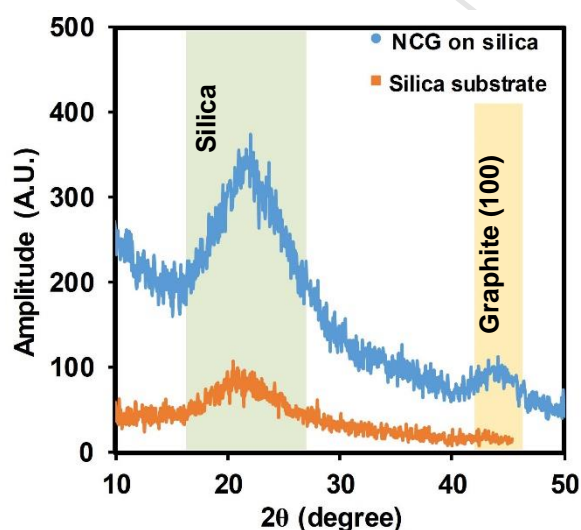

Fig. 6. X-ray diffraction patterns of the nanographite sample on fused silica substrate, and the bare silica substrate.

TEM analysis is shown in Fig. 7 (A-D), of an exfoliated flake suspended on a holey carbon grid. From the bright-field TEM images shown in Fig. 7(A-B), we observe that nanographite is comprised of planar sheets, randomly oriented. Fig. 7(C) is a HRTEM image, and here we observe nano-sized graphitic crystallite regions with no long-range order. The nano-scaled crystallites are of random orientation and range from a few to ~ 20 graphitic layers, which appears broadly consistent with the crystallite size obtained from XRD (~ 3 nm). The interlayer spacing d_{002} was measured using selected-area electron diffraction (SAED), Fig. 7 (D), and

10

shows interlayer graphite spacing of 0.34 nm, similar to previous measurements of between 0.34 and 0.345 nm [42,44] for nanographite. We were not able to calculate a value of (d_{002}) from XRD as this was largely masked by the substrate. The hexagonal spacing (d_{100}) was measured from SAED as 0.21 nm, in close agreement with the XRD value. The morphology of this nanographite is comparable to that observed in acidified sucrose-derived nanographite [42] in terms of crystallite size, interlayer spacing and random orientation.
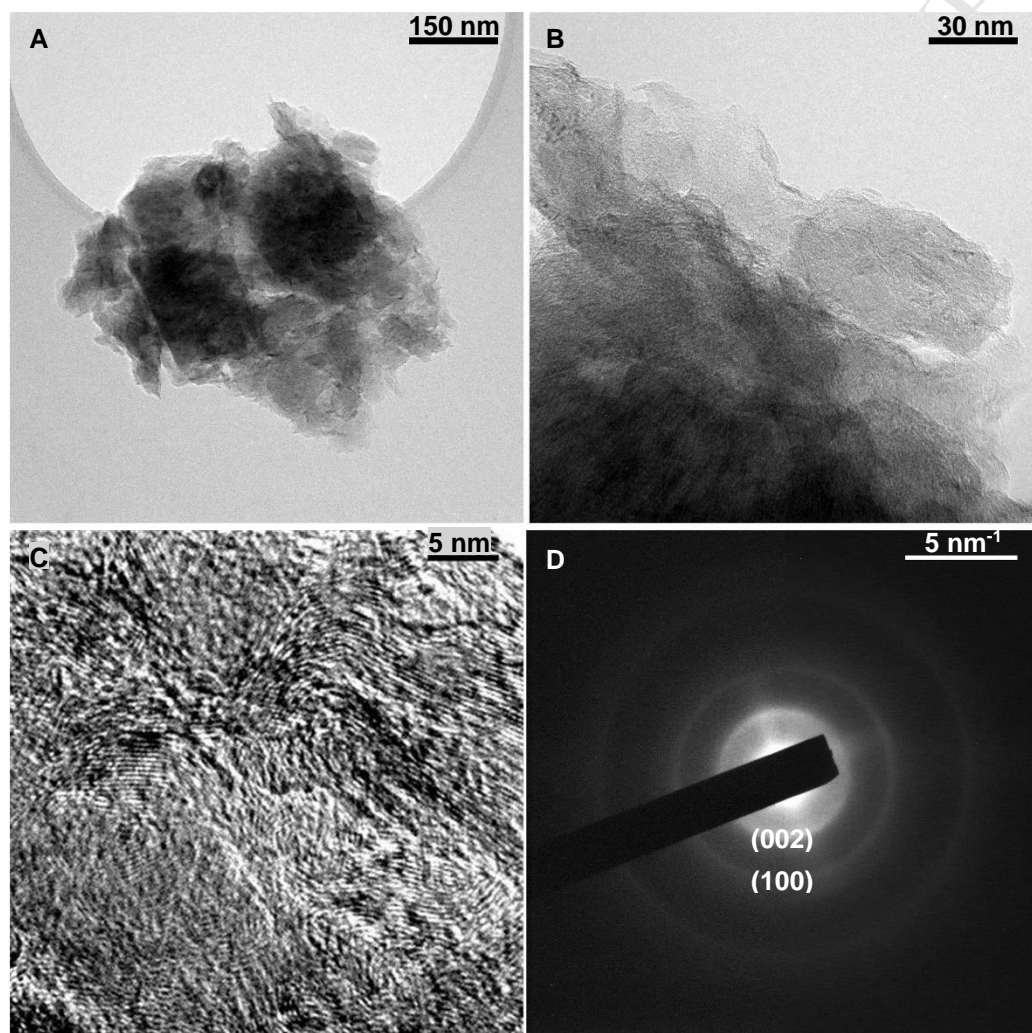
Fig. 7. (A-B) Bright field TEM images of nanographite sample suspended on a holey carbon grid (C) HRTEM images of a nanographite sample (D) Selected-area electron diffraction pattern, taken from the suspended region of the sample, shows hexagonal spacing (d_{100}) of 0.21 nm and interlayer spacing (d_{002}) of 0.34 nm.

1 The graphitic structure acts as a molecular sieve, as the interlayer spacing is small enough to
2 allow the flow of the smallest gases (helium, hydrogen and neon, summarised in Table 1), but
3 acts as a far greater barrier to larger gases such as CO_2 and O_2 [45–47]. Nanographite also
4 includes some amorphous bonding, but previous measurements have shown that amorphous
5 carbon does not have very high gas separation properties [15], with $\alpha^{H_2}/_{CO_2}$ measured at ~2.8
6 between the temperature range 25 to 250 °C and sieving is expected to be dominated by the
7 interlayer graphitic spacing. Previously the interlayer permeation of H_2 through pressed
8 graphite membranes was shown to have a significant effect on overall flow, in which the
9 permeation parallel to the grains was a factor of around 25 higher than that perpendicular to
10 the grains [5]. Shen *et al.* [47] showed that the 0.35 nm spacing between graphene oxide sheets
11 provided transport channels with high separation properties. However, for graphene-oxide, the
12 selectivity may also apparently be altered through different preparation techniques, Li *et al.*
13 [13] observed gas selectivity through a different mechanism of gas flow through pores and
14 defects at the grain boundaries with no major increase in flow observed with increased
15 interlayer spacing.

16   3.2   <u>Separation performance</u>

17 Initially, the single-gas permeance of helium, hydrogen and neon was measured through a
18 nanographite membrane over the temperature range 25 to 150 °C, with permeance values
19 shown in Fig. 8 (A). Note the much lower value of permeance for neon, as detailed in the inset
20 of Fig. 8(A). For each gas, the permeance increases exponentially with temperature. Fig. 8 (B)
21 is an Arrhenius plot showing the permeance against the inverse of temperature, which can be
22 used to calculate activation energy which is shown in Table 1.
23
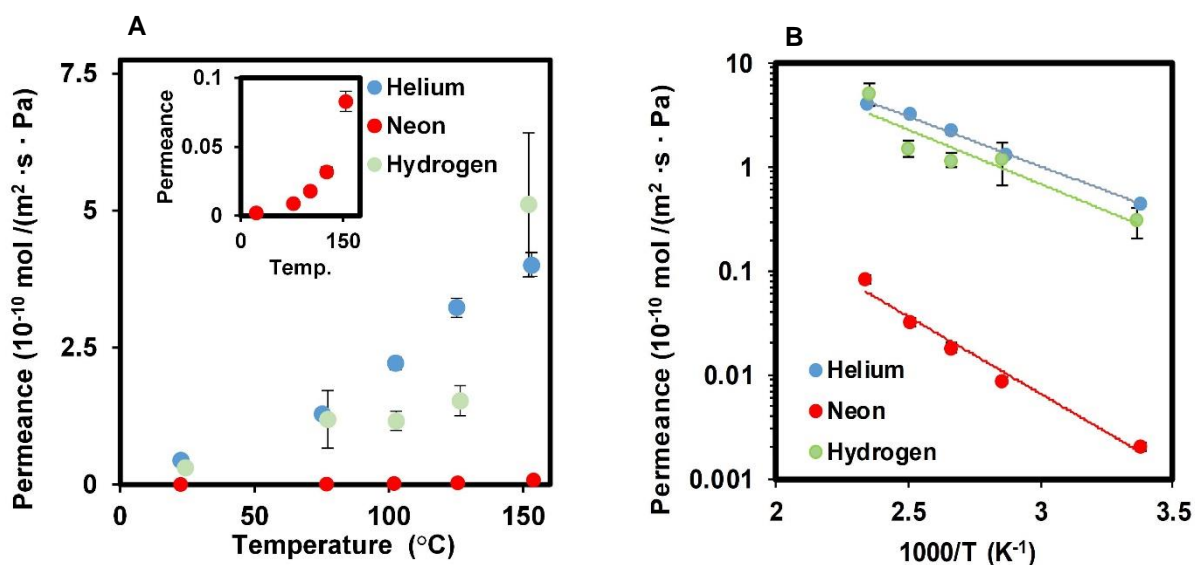
1

2 Fig. 8. (A) Measurement of the permeance of helium, hydrogen and neon through a 350 nm

3 thick nanographite membrane across the temperature range of 25 to 150 °C. Inset shows values

4 of neon permeance in detail, as the permeance is much lower than of the other gases. (B)

5 Arrhenius plot of the same data enables calculation of the activation energy of each gas.

6

Gas	Activation energy (kJ/Mol)	Molecular diameter (nm)
Helium	18.31	0.260 [48]
Hydrogen	20.03	0.289[48]
Neon	28.50	0.275[49]
Carbon Dioxide	-	0.339 [48]
Oxygen	-	0.346 [50]

7 Table 1. The calculated values of activation energy, and values of molecular diameter for five

8 measured gases.

9

10 The temperature dependent selectivity plot of $\alpha^{He}/_{Ne}$, and $\alpha^{H_2}/_{Ne}$ is shown in Fig. 9. At room

11 temperature $\alpha^{He}/_{Ne}$ and $\alpha^{H_2}/_{Ne}$ are 212 and 146, respectively. There is a clear decrease in the

12 selectivity as the temperature increases; with $\alpha^{He}/_{Ne} = 48$ and $\alpha^{H_2}/_{Ne} = 62$ at 150 °C. The reason

13 for this behaviour is simply that neon has a higher activation energy than helium or hydrogen,

14 and thus its permeance increases relatively more at higher temperatures.

1   To test the permeance of larger gases, the permeance of carbon dioxide and oxygen were

2   measured through a nanographite membrane. However, the permeation of both gases through

3   the nanographite membrane was below the limit of detection of the mass spectrometry system.

4   Low amounts of both gases were detected from the background of the UHV system (for

5   example CO_2 is known to diffuse from the inner steel walls [32]). However, the amount

6   diffusing through the membrane did not raise the measured value of either of these gases. As a

7   result, no absolute values of gas permeation and separation were obtained, but a lower limit for

8   separation factors of greater than ~135 and ~1000, respectively, can be ascertained for

9   hydrogen over both CO_2 and O_2, as any higher values would have been easily measured above

10   the background. This appears to indicate that there is a cut-off of permeance between hydrogen

11   (0.289 nm) and CO_2 (0.339 nm) as the permeance greatly differs between these two gases. This

12   may suggest that the flow of gases through nanographite is predominantly interlayer rather than

13   through inter-grain defects since the drop-off in permeance appears to lie close to the interlayer

14   spacing size (0.34 nm).

15
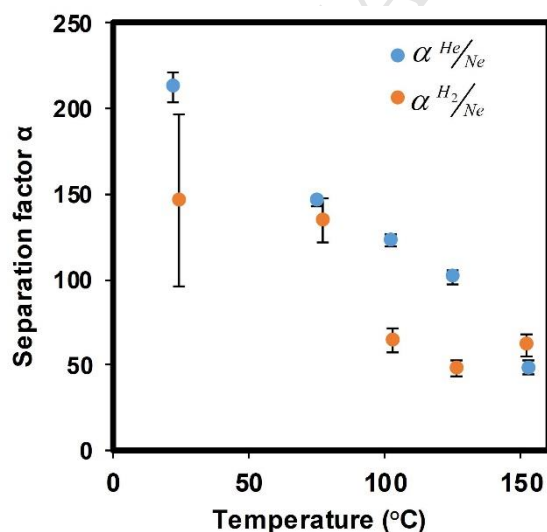
16   Fig. 9. Calculated values of separation factors $\alpha^{He}/_{Ne}$ and $\alpha^{H_2}/_{Ne}$ over the temperature range of

17   25 to 150 °C.

18   3.3   Discussion of separation behaviour

19   In inorganic membranes, the transport tends to be dominated by the following mechanisms:

20   Knudsen diffusion, surface diffusion, or sized-based molecular sieving (also termed gas

21   translation diffusion) [45,51–53]. In relatively large pores, the transport is dominated by the

22   mean-free-path of the molecule, which is known as Knudsen diffusion [51]. However, in the

23   present membranes, the ratio of permeance for both $\alpha^{He}/_{Ne}$ and $\alpha^{H_2}/_{Ne}$ is far higher than that

14

predicted by Knudsen diffusion, which may be calculated from the molecular mass M of either constituent, for example ($\alpha_{Knudsen}\ ^{He}/_{Ne} = \sqrt{M_{Neon} / M_{Helium}} = 2.2$). For smaller pores, the flow may be dominated by surface diffusion [45] where molecules adsorb on to the pore walls, before hopping to the next available site [49]. As temperature increases, the adsorption decreases and thus the permeance from surface diffusion flow will also decrease [54], which is not observed in any significant way in our data.

Hence, for the nanographite membrane, the flow is probably dominated by molecular sieving (gas translation diffusion) for the smallest pores as has been previously noted in various carbon-based membranes [45,52]. In gas translational diffusion, there is an activated step where the molecule must overcome an energy barrier imposed by the surface potential of the pore walls, followed by gas-state diffusion in a Knudsen-type regime [53]. From our Arrhenius plot, the negative slope of the Arrhenius plot indicates that gas translation separation mechanism dominates the flow [45,49]. However, this is not to say surface diffusion is not present. Membranes often have transport with a combination of surface diffusion and gas translation diffusion [54,55] where the surface diffusion becomes less dominant, or negligible, at higher temperatures, as the adsorption decreases. More highly-adsorbing gases have a higher surface diffusion gas flow [49].

Molecular sieving in many types of graphitic membranes has been observed in the literature, and tends to be described as arising from two main types of structure: (I) in some graphene oxide materials, the sieving is dominated by inter-grain defects and with no apparent major change in permeation characteristics when the interlayer spacing is increased [13], and (II) where sieving is dominated by the interlayer spacing between sheets, whereby smaller molecules can pass between stacked sheets but larger molecules cannot [5,16,47] and thus the larger gases have a much lower permeance. Ibrahim *et al.* [56] recently proposed a two-pathway transport model in graphene oxide, whereby there are inter-sheet pathways composed of nanoscale wrinkles between sheets, and inner-sheet pathways consisting of structural defects in the sheets.

In nanographite, the mechanism shows evidence of being dominated by interlayer spacing, as explained here. We note that neon has a significantly lower permeation, Fig 8, than hydrogen through nanographite membranes, despite being a smaller molecule (0.275 vs 0.289 nm

diameter [48,49]). Similar behaviour has been observed in carbon [5,57] and silica membranes [49,58], where for example, hydrogen has much higher permeance than helium or neon. This behaviour may be explained by the higher relative adsorption of hydrogen compared to neon, which has been measured in porous carbons [59,60] which are comparable to nanographite. Thus at lower temperatures, hydrogen has a larger component of gas-flow which is caused by surface diffusion than neon does. At higher temperatures the adsorption of hydrogen will become less or negligible [59,60] and therefore as the temperature increases, the flow of hydrogen that is caused by surface-diffusion becomes smaller, but this effect is not so strong in neon since the adsorption is relatively small. At higher temperatures, for all gases, any component of transport caused by surface diffusion will become small and the mechanism will turn to pure sized-based molecular sieving, for all gases which is in suggested by the decrease in $\alpha^{H_2}/_{Ne}$ at higher temperatures, Fig. 9.

The higher selectivity of hydrogen over neon further suggests that nanographite has an interlayer sieving mechanism as opposed to inter-grain defect mechanism. Channels formed by interlayer defects tend to have a longer length (~ equal to the crystallite size) than inter-grain defects which tend to be through just one atomic layer [11]. Longer channels provide many adsorption sites, thus allowing significant differential absorption of hydrogen compared to neon, whereas inter-grain defects tend to act solely on size-based sieving [13].

We note that the absolute gas permeance of these membranes is relatively low compared with values found in much of the available literature (Table 2), which is a crucial parameter for membranes to be used in industrial gas separation applications. However, the low permeance of these membranes may largely be explained by the relatively high thickness of these particular samples (350 nm). These were fabricated to this thickness to ensure sufficient strength in order to protect our UHV system from any unintended membrane failure (which we did not observe throughout testing). In other work we have deposited continuous nanographite films of sub-10 nm thickness, for electronic applications [61,62] and this fabrication method for membranes may potentially be carried out on such thin films. If sufficiently robust 10 nm thick membranes could be fabricated, the expected hydrogen permeance would of order $\sim 2 \times 10^{-8}$ mol $\cdot$ m^{-2} $\cdot$ s^{-1} $\cdot$ Pa^{-1} at 150 °C. Further improvements could be made by using nanographite in a mixed-matrix membrane as shown recently in graphene oxide membranes

1 [63,64] where permeance and mechanical stability was increased by blending graphene oxide

2 with polymer.

3

4 The coefficient of permeability C (Equation 4) is a measure of the thickness-normalised

5 permeance, and hence allows better comparison between materials than the absolute

6 permeance. The calculated values of C for hydrogen through nanographite are comparable to

7 related materials such as graphene oxide [13], as detailed in Table 2. Comparing these materials

8 on both permeability and $\alpha^{H_2}/_{CO_2}$ shows that nanographite compares favourably, though we

9 clearly note that further measurement of the absolute permeance of a wider range of gases will

10 be useful. We also include the sieving performance of $\alpha^{He}/_{Ne}$ and $\alpha^{H_2}/_{O_2}$, since these gases are

11 more commonly measured in the literature than $\alpha^{He}/_{Ne}$, for a comparison with a number of

12 other materials. The nanographite membrane consistently shows high separation properties.

13

1

Material	Test temp. (°C)	H_2 permeance (mol · m^{-2} ·s^{-1} · Pa^{-1})	Sample thickness (μm)	H_2 Permeability (mol · m ·m^{-2} · s^{-1} · Pa^{-1})	$\alpha^{H_2}/_{CO_2}$	$\alpha^{He}/_{Ne}$	$\alpha^{H_2}/_{O_2}$
Nanographite [This work]	125	1.53×10^{-10}	0.350	5.35×10^{-17}	> 135	48	-
Nanographite [This work]	150	5.11×10^{-10}	0.350	1.79×10^{-16}	-	62	>1000
Pressed graphite [5]	150	7.1×10^{-9}	1000	7.1×10^{-12}	~ 4.7	-	-
Graphene-oxide [13]	100	2.0×10^{-7}	0.0018	3.7×10^{-16}	~ 22	-	-
Turbostratic carbon [15]	150	5.7×10^{-9}	~8	4.6×10^{-14}	~ 4.7	-	-
Carbon hollow fiber membranes: [57]	60	1.5×10^{-9}	100	1.5×10^{-13}	8.40	-	55
Silica membranes [65]	200	5.5×10^{-8}	0.2	1.1×10^{-14}	-	10.5	-

2

3 Table 2. Summary of the hydrogen permeance and permeation properties and separation

4 between various gases of a number of membranes from the available literature.

5 **4 Conclusions**

6 We have reported for the first time the preparation and permeance testing of freestanding,

7 350 nm thick, nanographite thin film membranes, produced using PECVD. The method used

8 to fabricate these membranes is scalable and reproducible, using micromachining and deep

9 etching of fused silica wafers. A UHV-based mass spectrometry system is used to measure the

10 permeance of various gases through the membrane and the results show a predominantly gas

11 translation-type permeance behaviour. The gas permeability coefficient of helium and

12 hydrogen is similar to that of related materials such as graphene oxide, however the separation

13 factors of nanographite at elevated temperatures are far higher and in particular, the separation

18

1 of $\alpha^{He}/_{Ne}$ equals 48 at 150 °C, $\alpha^{H_2}/_{CO_2}$ >135 at 125 °C and $\alpha^{H_2}/_{O_2}$ >1000 at 150 °C. The high

2 $\alpha^{H_2}/_{CO_2}$, large scale and inexpensive synthesis route, and compatibility for microfabrication

3 show nanographite to be a promising material for micro-scaled membrane applications.

5 Acknowledgements

6 References

12 [1] J. Sunarso, S.S. Hashim, Y.S. Lin, S.M. Liu, Membranes for helium recovery: An
13 overview on the context, materials and future directions, Separation and Purification
14 Technology. 176 (2017) 335–383. doi:10.1016/j.seppur.2016.12.020.

15 [2] N.W. Ockwig, T.M. Nenoff, Membranes for hydrogen separation, Chemical Reviews.
16 107 (2007) 4078–4110. doi:10.1021/cr0501792.

17 [3] Z. Cai, R.H. Clarke, B.A. Glowacki, W.J. Nuttall, N. Ward, Ongoing ascent to the
18 helium production plateau-Insights from system dynamics, Resources Policy. 35 (2010)
19 77–89. doi:10.1016/j.resourpol.2009.10.002.

20 [4] W.J. Nuttall, R.H. Clarke, B.A. Glowacki, Resources: Stop squandering helium, Nature.
21 485 (2012) 573–575. doi:10.1038/485573a.

22 [5] A. Schulz, F. Steinbach, J. Caro, Pressed graphite crystals as gas separation membrane
23 for steam reforming of ethanol, Journal of Membrane Science. 469 (2014) 284–291.
24 doi:10.1016/j.memsci.2014.06.047.

25 [6] C. Huang, H. Wu, K. Deng, W. Tang, E. Kan, Improved permeability and selectivity in
26 porous graphene for hydrogen purification, Phys. Chem. Chem. Phys. 16 (2014) 25755–
27 25759. doi:10.1039/C4CP04385E.

28 [7] J. Schrier, Helium separation using porous graphene membranes, Journal of Physical
29 Chemistry Letters. 1 (2010) 2284–2287. doi:10.1021/jz100748x.

1   [8]   M. Bartolomei, E. Carmona-Novillo, M.I. Hernández, J. Campos-Martínez, F. Pirani,
2   G. Giorgi, Graphdiyne pores: Ad hoc openings for helium separation applications,
3   Journal of Physical Chemistry C. 118 (2014) 29966–29972. doi:10.1021/jp510124e.

4   [9]   F. Li, Y. Qu, M. Zhao, Efficient helium separation of graphitic carbon nitride membrane,
5   Carbon. 95 (2015) 51–57. doi:10.1016/j.carbon.2015.08.013.

6   [10] W. Hu, X. Wu, Z. Li, J. Yang, Helium separation via porous silicene based ultimate
7   membrane, Nanoscale. 5 (2013) 9062–9066. doi:10.1039/C3NR02326E.

8   [11] M.S.H. Boutilier, C. Sun, S.C. O'Hern, H. Au, N.G. Hadjiconstantinou, R. Karnik,
9   Implications of permeation through intrinsic defects in graphene on the design of defect-
10   tolerant membranes for gas separation, ACS Nano. 8 (2014) 841–849.
11   doi:10.1021/nn405537u.

12 [12] H.W. Kim, H.W. Yoon, S. Yoon, B.M. Yoo, B.K. Ahn, Y.H. Cho, *et al.*, Selective Gas
13   Transport Through few-layered graphene and graphene oxide membranes, Science. 342
14   (2013) 91–95. doi:10.1126/science.1236098.

15 [13] H. Li, Z. Song, X. Zhang, Y. Huang, S. Li, Y. Mao, *et al.*, Ultrathin, Molecular-Sieving
16   Graphene Oxide Membranes for Selective Hydrogen Separation, Science. 342 (2013)
17   95–98. doi:10.1126/science.1236686.

18 [14] C. Chi, X. Wang, Y. Peng, Y. Qian, Z. Hu, J. Dong, *et al.*, Facile Preparation of
19   Graphene Oxide Membranes for Gas Separation, Chemistry of Materials. 28 (2016)
20   2921–2927. doi:10.1021/acs.chemmater.5b04475.

21 [15] A. Wollbrink, K. Volgmann, J. Koch, K. Kanthasamy, C. Tegenkamp, Y. Li, H. Richter,
22   *et al.*, Amorphous, turbostratic and crystalline carbon membranes with hydrogen
23   selectivity, Carbon. 106 (2016). doi:http://dx.doi.org/10.1016/j.carbon.2016.04.062.

24 [16] E.A. Efimova, D.A. Syrtsova, V. V. Teplyakov, Gas permeability through graphite foil:
25   The influence of physical density, membrane orientation and temperature, Separation
26   and Purification Technology. 179 (2017) 467–474. doi:10.1016/j.seppur.2017.02.023.

27 [17] Y. Yang, P. Dementyev, N. Biere, D. Emmrich, P. Stohmann, R. Korzetz, *et al.*, Rapid
28   Water Permeation Through Carbon Nanomembranes with Sub-Nanometer Channels,
29   ACS Nano. Article (2018). doi:10.1021/acsnano.8b01266.

30 [18] J.B.S. Hamm, A.R. Muniz, L.D. Pollo, N.R. Marcilio, I.C. Tessaro, Experimental and
31   computational analysis of carbon molecular sieve membrane formation upon
32   polyetherimide pyrolysis, Carbon. 119 (2017) 21–29.
33   doi:10.1016/j.carbon.2017.04.011.

34 [19] M.J. Varady, L. McLeod, J.M. Meacham, F.L. Degertekin, A.G. Fedorov, An integrated

20

MEMS infrastructure for fuel processing: Hydrogen generation and separation for portable power generation, Journal of Micromechanics and Microengineering. 17 (2007). doi:10.1088/0960-1317/17/9/S08.

[20] T. Boeltken, A. Wunsch, T. Gietzelt, P. Pfeifer, R. Dittmeyer, Ultra-compact microstructured methane steam reformer with integrated Palladium membrane for on-site production of pure hydrogen: Experimental demonstration, International Journal of Hydrogen Energy. 39 (2014) 18058–18068. doi:10.1016/j.ijhydene.2014.06.091.

[21] B.A. Wilhite, S.E. Weiss, J.Y. Ying, M.A. Schmidt, K.F. Jensen, High-purity hydrogen generation in a microfabricated 23 wt % Ag-Pd membrane device integrated with 8:1 $LaNi_{0.95}Co_{0.05}O_3/Al_2O_3$ catalyst, Advanced Materials. 18 (2006) 1701–1704. doi:10.1002/adma.200502025.

[22] H. Medina, Y.-C.C. Lin, C.H. Jin, C.-C.C. Lu, C.-H.H. Yeh, K.-P.P. Huang, *et al.*, Metal-Free Growth of Nanographene on Silicon Oxides for Transparent Conducting Applications, Advanced Functional Materials. 22 (2012) 2123–2128. doi:10.1002/adfm.201102423.

[23] L. Zhang, Z. Shi, Y. Wang, R. Yang, D. Shi, G. Zhang, Catalyst-free growth of nanographene films on various substrates, Nano Research. 4 (2010) 315–321. doi:10.1007/s12274-010-0086-5.

[24] M.E. Schmidt, C. Xu, M. Cooke, H. Mizuta, H.M.H. Chong, Metal-free plasma-enhanced chemical vapor deposition of large area nanocrystalline graphene, Materials Research Express. 1 (2014) 025031. doi:10.1088/2053-1591/1/2/025031.

[25] S.J. Fishlock, D. Grech, J.W. McBride, H.M.H. Chong, S.H. Pu, Mechanical characterisation of nanocrystalline graphite using micromechanical structures, Microelectronic Engineering. 159 (2016) 184–189. doi:10.1016/j.mee.2016.03.040.

[26] S.J. Fishlock, S.J. O'Shea, J.W. McBride, H.M.H. Chong, S.H. Pu, Fabrication and characterisation of nanocrystalline graphite MEMS resonators using a geometric design to control buckling, Journal of Micromechanics and Microengineering. 27 (2017). doi:10.1088/1361-6439/aa7ebb.

[27] J.-Y. Jin, S. Yoo, J.-S. Bae, Y.-K. Kim, Deep wet etching of borosilicate glass and fused silica with dehydrated AZ4330 and a Cr/Au mask, Journal of Micromechanics and Microengineering. 24 (2014) 015003. doi:10.1088/0960-1317/24/1/015003.

[28] P. Tremblay, M. Savard, J. Vermette, R. Paquin, Gas permeability, diffusivity and solubility of nitrogen, helium, methane, carbon dioxide and formaldehyde in dense polymeric membranes using a new on-line permeation apparatus, Journal of Membrane

21

1   Science. 282 (2006) 245–256. doi:10.1016/j.memsci.2006.05.030.

2   [29]   G. Firpo, E. Angeli, L. Repetto, U. Valbusa, Permeability thickness dependence of

3   polydimethylsiloxane (PDMS) membranes, Journal of Membrane Science. 481 (2015)

4   1–8. doi:10.1016/j.memsci.2014.12.043.

5   [30]   O.B. Malyshev, K.J. Middleman, In situ ultrahigh vacuum residual gas analyzer

6   "calibration," Journal of Vacuum Science & Technology A. 26 (2008) 1474–1479.

7   doi:10.1116/1.2990856.

8   [31]   C.D. Ehrlich, J.A. Basford, Recommended practices for the calibration and use of leaks,

9   Journal of Vacuum Science & Technology A. 10 (1992) 1–17. doi:10.1116/1.578137.

10   [32]   Y. Ishikawa, T. Yoshimura, Importance of the surface oxide layer in the reduction of

11   outgassing from stainless steels, Journal of Vacuum Science & Technology A. 13 (1995)

12   1847–1852. doi:10.1116/1.579669.

13   [33]   Y. Li, F. Liang, H. Bux, W. Yang, J. Caro, Zeolitic imidazolate framework ZIF-7 based

14   molecular sieve membrane for hydrogen separation, Journal of Membrane Science. 354

15   (2010) 48–54. doi:10.1016/j.memsci.2010.02.074.

16   [34]   Table of units, Journal of Membrane Science. 366 (2011) III–III. doi:10.1016/S0376-

17   7388(10)00894-X.

18   [35]   W. Yang, C. He, L. Zhang, Y. Wang, Z. Shi, M. Cheng, *et al.*, Growth, characterization,

19   and   properties   of   nanographene.,   Small.   8   (2012)   1429–35.

20   doi:10.1002/smll.201101827.

21   [36]   J. Sun, M.E. Schmidt, M. Muruganathan, H.M.H. Chong, H. Mizuta, Large-scale

22   nanoelectromechanical switches based on directly deposited nanocrystalline graphene

23   on insulating substrates, Nanoscale. 8 (2016) 6659–6665. doi:10.1039/C6NR00253F.

24   [37]   A.C. Ferrari, J. Robertson, Interpretation of Raman spectra of disordered and amorphous

25   carbon, Physical Review B. 61 (2000) 14095–14107. doi:10.1103/PhysRevB.61.14095.

26   [38]   T.M.G. Mohiuddin, A. Lombardo, R.R. Nair, A. Bonetti, G. Savini, R. Jalil, *et al.*,

27   Uniaxial strain in graphene by Raman spectroscopy: G peak splitting, Grüneisen

28   parameters,   and   sample   orientation,   Physical   Review   B.   79   (2009)   205433.

29   doi:10.1103/PhysRevB.79.205433.

30   [39]   E.H. Martins Ferreira, M.V.O. Moutinho, F. Stavale, M.M. Lucchese, R.B. Capaz, C.A.

31   Achete, *et al.*, Evolution of the Raman spectra from single-, few-, and many-layer

32   graphene with increasing disorder, Physical Review B - Condensed Matter and Materials

33   Physics. 82 (2010). doi:10.1103/PhysRevB.82.125429.

34   [40]   Q. Nian, Y. Wang, Y. Yang, J. Li, M.Y. Zhang, J. Shao, *et al.*, Direct laser writing of

nanodiamond films from graphite under ambient conditions, Scientific Reports. 4 (2014) 1–8. doi:10.1038/srep06612.

[41] B.D. Cullity, Elements of X-ray Diffraction, Third Edition, Prentice-Hall, New York, USA, 2001.

[42] N.J. Hargreaves, S.J. Cooper, Nanographite Synthesized from Acidified Sucrose Microemulsions under Ambient Conditions, Crystal Growth and Design. 16 (2016) 3133–3142. doi:10.1021/acs.cgd.5b01753.

[43] A.L. Patterson, The Scherrer formula for X-ray particle size determination, Physical Review. 56 (1939) 978. doi:10.1103/PhysRev.56.978.

[44] V.Y. Osipov, T. Enoki, K. Takai, K. Takahara, M. Endo, T. Hayashi, *et al.*, Magnetic and high resolution TEM studies of nanographite derived from nanodiamond, Carbon. 44 (2006) 1225–1234. doi:10.1016/j.carbon.2005.10.047.

[45] J. Gilron, A. Soffer, Knudsen diffusion in microporous carbon membranes with molecular sieving character, Journal of Membrane Science. 209 (2002) 339–352. doi:10.1016/S0376-7388(02)00074-1.

[46] R.S.A. De Lange, K. Keizer, A.J.J. Burggraaf, R.S.A. de Lange, K. Keizer, A.J.J. Burggraaf, Analysis and theory of gas transport in microporous sol-gel derived ceramic membranes, Journal of Membrane Science. 104 (1995) 81–100. doi:10.1016/0376-7388(95)00014-4.

[47] J. Shen, G. Liu, K. Huang, W. Jin, K.R. Lee, N. Xu, Membranes with fast and selective gas-transport channels of laminar graphene oxide for efficient CO_2 capture, Angewandte Chemie - International Edition. 54 (2015) 578–582. doi:10.1002/anie.201409563.

[48] H.L. Castricum, H.F. Qureshi, A. Nijmeijer, L. Winnubst, Hybrid silica membranes with enhanced hydrogen and CO_2 separation properties, Journal of Membrane Science. 488 (2015) 121–128. doi:10.1016/j.memsci.2015.03.084.

[49] W.J.W. Bakker, L.J.P. Van Den Broeke, F. Kapteijn, J.A. Moulijn, Temperature dependence of one-component permeation through a silicalite-1 membrane, AIChE Journal. 43 (1997) 2203–2214. doi:10.1002/aic.690430907.

[50] W.J. Koros, G.K. Fleming, Membrane-based gas separation, Journal of Membrane Science. 83 (1993) 1–80. doi:10.1016/0376-7388(93)80013-N.

[51] P. Pandey, R.S. Chauhan, Membranes for gas separation, Progress in Polymer Science. 26 (2001) 853–893. doi:10.1016/S0079-6700(01)00009-0.

[52] A.W. Thornton, A. Ahmed, S.K. Kannam, B.D. Todd, M. Majumder, A.J. Hill, Analytical Diffusion Mechanism (ADiM) model combining specular, Knudsen and

surface diffusion, Journal of Membrane Science. 485 (2015) 1–9. doi:10.1016/j.memsci.2015.03.004.

[53] S.B. Messaoud, A. Takagaki, T. Sugawara, R. Kikuchi, S.T. Oyama, Alkylamine-silica hybrid membranes for carbon dioxide/methane separation, Journal of Membrane Science. 477 (2015) 161–171. doi:10.1016/j.memsci.2014.12.022.

[54] J.C. Poshusta, R.D. Noble, J.L. Falconer, Temperature and pressure effects on CO_2 and CH_4 permeation through MFI zeolite membranes, Journal of Membrane Science. 160 (1999) 115–125. doi:10.1016/S0376-7388(99)00073-3.

[55] P.F. Zito, A. Caravella, A. Brunetti, E. Drioli, G. Barbieri, Knudsen and surface diffusion competing for gas permeation inside silicalite membranes, Journal of Membrane Science. 523 (2017) 456–469. doi:10.1016/j.memsci.2016.10.016.

[56] A. Ibrahim, Y.S. Lin, Gas permeation and separation properties of large-sheet stacked graphene oxide membranes, Journal of Membrane Science. 550 (2018) 238–245. doi:10.1016/j.memsci.2017.12.081.

[57] E.P. Favvas, N.S. Heliopoulos, S.K. Papageorgiou, A.C. Mitropoulos, G.C. Kapantaidakis, N.K. Kanellopoulos, Helium and hydrogen selective carbon hollow fiber membranes: The effect of pyrolysis isothermal time, Separation and Purification Technology. 142 (2015) 176–181. doi:10.1016/j.seppur.2014.12.048.

[58] S.T. Oyama, D. Lee, P. Hacarlioglu, R.F. Saraf, Theory of hydrogen permeability in nonporous silica membranes, Journal of Membrane Science. 244 (2004) 45–53. doi:10.1016/j.memsci.2004.06.046.

[59] R.M. Barrer, E. Strachan, Sorption and Surface Diffusion in Microporous Carbon Cylinders, Proceedings of the Royal Society of London A: Mathematical, Physical and Engineering Sciences. 231 (1955) 52–74. doi:10.1098/rspa.1955.0156.

[60] C.K. Chan, E. Tward, K.I. Boudaie, Adsorption isotherms and heats of adsorption of hydrogen, neon and nitrogen on activated charcoal, Cryogenics. 24 (1984) 451–459. doi:10.1016/0011-2275(84)90001-8.

[61] T.Y. Ling, S.J. Fishlock, M.S. Shamsudin, S.M. Sultan, H.M.H. Chong, S.H. Pu, Design and fabrication of a nanocrystalline graphite thin-film sensor for in situ ionic concentration monitoring, in: Proceedings of IEEE Sensors, 2017. doi:10.1109/ICSENS.2017.8234336.

[62] S.M. Sultan, S.H. Pu, S.J. Fishlock, L.H. Wah, H.M.H. Chong, J.W. McBride, Electrical behavior of nanocrystalline graphite/p-Si Schottky diode, in: 2016 IEEE 16th International Conference on Nanotechnology (IEEE-NANO), 2016: pp. 307–310.

24

1   doi:10.1109/NANO.2016.7751379.

2 [63] Z. Wang, H. Yu, J. Xia, F. Zhang, F. Li, Y. Xia, Y. Li, Novel GO-blended PVDF
3   ultrafiltration membranes, Desalination. 299 (2012) 50–54.
4   doi:10.1016/j.desal.2012.05.015.

5 [64] S. Castarlenas, C. Téllez, J. Coronas, Gas separation with mixed matrix membranes
6   obtained from MOF UiO-66-graphite oxide hybrids, Journal of Membrane Science. 526
7   (2017) 205–211. doi:10.1016/j.memsci.2016.12.041.

8 [65] S.J. Ahn, G.N. Yun, A. Takagaki, R. Kikuchi, S.T. Oyama, Synthesis and
9   characterization of hydrogen selective silica membranes prepared by chemical vapor
10   deposition of vinyltriethoxysilane, Journal of Membrane Science. 550 (2018) 1–8.
11   doi:10.1016/j.memsci.2017.12.038.

12